RIGA TECHNICAL UNIVERSITY

Faculty of Materials Science and Applied Chemistry

Violeta Carrillo Rodrigo

Student in the Erasmus program

PREPARATION AND CHARACTERIZATION OF TiO$_2$-SiO$_2$-ZnO-SnO$_2$-Fe$_2$O$_3$ SOL-GEL COATINGS

Master Thesis

Scientific advisor:

Dr.sc.eng., leading researcher

Ilona Pavlovska

Scientific consultant:

Mg.sc., assistant Anzelms Zukuls

Riga   2017

RIGA TECHNICAL UNIVERSITY

Faculty of Materials Science and Applied Chemistry

Institute of Silicate Materilas

Leading researcher, Dr.sc.eng.:

_____I.Pavlovska

September 2, 2016

Tasks of Master Thesis to

AKBK0 Master programm student **Carrillo Rodrigo Violeta** stud. N° 161AKB007.

Title of Master Thesis: **PREPARATION AND CHARACTERIZATION OF TiO_2-SiO_2-ZnO-SnO_2-Fe_2O_3 SOL-GEL COATINGS.**

Literature review

Explore and summarize the latest available literature (from 2005 to 2016) on TiO_2, SiO_2, ZnO, SnO_2, Fe_2O_3 base and its composite systems, their properties and applications. Get an idea of the surface-active substances to modify the surface of the coatings.

Methodological part

Describe about all investigation method used in the Master Thesis. Explain preparation technique for the sols, preparation of substrates before dip-coating, necessary calculation methods used.

Experimental part

With the sol-gel dip-coating method obtain homogeneous coatings without cracks using slow and fast withdrawal rates (60 mm/min and 220 mm/min, respectively); confirm the absence of cracks by optical microscopy. Determine the crystal phase and crystal size by X-ray analysis; investigate the morphology of the coatings by atomic force microscopy and scanning electron microscopy. Verify the photocatalytical activity of prepared coating in UV-vis region.

_____ **/Carrillo Rodrigo Violeta/**

(*signature*)

Master Thesis has been developed and completely written on January 27, 2017 at Riga Technical University Faculty of Materials Science and Applied Chemistry Institute of Silicate Materials with the mark ____.

Author: *Carrillo Rodrigo Violeta*..

                                                                                        (Signature)

Scientific advisor: *Ilona Pavlovska*..

                                                                                        (Signature)

Scientific consultant: *Anzelms Zukuls*..

                                                                                        (Signature)

ABSTRACT

The Master's Thesis is about the preparation and characterization of different systems withinTiO$_2$-SiO$_2$-ZnO-SnO$_2$-Fe$_2$O$_3$ system. The available information about all precursors, dip-coating technique, drying and sintering as well as their preparation methods were processed in this study.

In the experimental part, by the sol-gel dip-coating method the coating systems of three, four and five components sol-gel coatings on the glass substrate were obtained. Using OM, X-ray, AFM and SEM the affecting factors and concepts of coating systems, as microstructure, phase composition, surface morphology and the photocatalytic activity of resulting were investigated.

The Master's thesis consists of 95 pages, contains 52 figures, 10 tables, 1 appendix and 133 references.

RESUMEN

La Máster Tesis trata sobre la preparación y caracterización de diferentes sistemas con TiO_2-SiO_2-ZnO-SnO_2-Fe_2O_3. Para ello, toda la información disponible sobre los precursores, la técnica de dip-coating, el secado y el sinterizado así como los métodos de preparación han sido recogidos en este estudio.

En la parte experimental, se han realizado mediante el método sol-gel y la técnica de dip-coating los diferentes sistemas con tres, cuatro y cinco componentes sobre sustratos de vidrio. Empleando OM, X-ray, AFM, SEM se han investigado los factores y conceptos que afectan a la microestructura, la composición de las fases, la morfología de la superficie y la actividad fotocatalítica.

La Máster Tesis consta de 95 páginas, 52 figures, 10 tablas, 1 apéndice y 133 referencias.

ABBREVIATIONS

TiEt	Titanium (IV) ethoxide
TEOS	Tetraethyl ortosilicate
ZnAc	Zinc acetate
$SnCl_4$	Tin (IV) chloride pentahydrate
FeAc	Iron (II) acetate
DEA	Diethanolamine
PVP	Polyvinylpyrrolidone
PEG	Polyethylenglycol
DTAB	Dodecyltrimethylammonium bromide
CTAB	Hexadecyltrimethylammonium bromide
TTAB	Myristyltrimethylammonium bromide
SDS	Sodium dodecyl sulphate
CVD	Chemical vapour deposition
XRD	X-ray diffraction
FTIR	Fourier transform infrared spectroscopy
EDS	Energy-dispersive X-ray spectroscopy
SEM	Scanning electron microscopy
UV	Ultraviolet
OM	Optical microscopy
AFM	Atomic force microscopy
MO	Methyl orange
US	Ultrasonic

CONTENTS

1. LITERATURE REVIEW

1.1.SOL-GEL PROCESSING

Interest in the sol-gel processing of inorganic ceramic and glass materials began in mid-1800s with Ebelman and Graham's studies on silica gels. And after a time period, between 1800s and 1920s, gels became considerable interest to chemists stimulated by the phenomenon of Liesegang Rings formed from gels. [1] Currently the sol process is used by a high number of materials science researchers because its versatility allows the preparation of a large number of materials. [2]
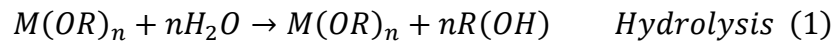
A colloid is a suspension in which the dispersed phase is so small (~1-1000 nm) that gravitational forces are negligible and interactions are dominated by short-range forces, such as van der Waals attraction and surface charges. Also, the inertia of the dispersed phase is small enough that it exhibits Brownian motion, the random motion of particles suspended in a fluid (liquid or gas) resulting from their collision with the fast-moving atoms or molecules in the fluid. [3] There are different types of colloids: sol, aerosol and emulsion. The sol is a suspension with solid particles in a liquid, the aerosol is like a sol but the particles are suspended in a gas and the emulsion is a suspension of liquid droplets in another liquid. All of these types of colloids can be used to generate polymers or particles from which ceramic materials can be made.

In the sol-gel process, precursors (starting compounds) are needed; they consist in a metal or metalloid element surrounded by various ligands (appendages not including another metal or metalloid atom). [3]

There are two ways to prepare sol-gel coatings: the inorganic method and organic method. The inorganic method involves the evolution of networks through the formation of a colloidal suspension (usually oxides) and gelation of the sol (colloidal suspension of very small particles, 1-100 nm) to form a network in continuous liquid phase. But the most common is the organic, which starts with a solution of monomers; ideal monomers are molecules which form $M - O - M$ units ($M = metal$), like metal alkoxides, $M(OR)_n$ where R is an alkyl radical. The metal alkoxides are dissolved in alcohol or other low-molecular weight organic solvent. [4] [2]

Generally the sol-gel formation occurs in four stages: (1) hydrolysis, (2) condensation and polymerization of monomers to form chains and particles, (3) growth of the particles, (4) agglomeration of the polymer structures followed by the formation of networks that extend

throughout the liquid medium resulting in thickening, which forms a gel. However, hydrolysis and condensation occurs at the same time, once hydrolysis has been started; so the reactions can be summarized in these equations [2] [5]:

$$M(OR)_n + nH_2O \rightarrow M(OR)_n + nR(OH) \qquad Hydrolysis \ (1)$$

$$M(OR)_n \rightarrow MO_{n/2} + \frac{n}{2}H_2O \qquad Polycondensation \ (2)$$

The reactions are affected by the initial reaction conditions, such as pH, temperature, molar ratios of reactants, solvent compositions, etc. [4]

1.2. RAW MATERIALS

To decide the materials in which this project is based, are used different compositions of precursors; however in the literature appears others that are useful and have good properties (Table 1).

Table 1. Summary table of different compositions.

Composition	Methods	Properties	Reference
TiO_2	-Dip-coating -Spin-coating -Electrospinning	-Crystalline phase (anatase, rutile) -Small particle size (~93-495 nm) -High contact angle (~65°-92°) -High Transmittance (~90%) -High transparency -Good photocatalytic activity (MO 87 and 50% for 6h, MB50% for 3h) -High reflectance	[6], [7], [8], [9], [10], [11], [12], [13]
SiO_2	-Dip-coating -Spin-coating -Sol-gel	-High transmittance and conductivity -Corrosion protection -Porous structures	[14], [15], [16], [17], [18], [19], [20], [21],
ZnO	-Dip-coating -Sol-gel synthesis (powder) -Spin-coating -Hydrothermal deposition	-Crystalline phase (zincite, cubic phase, hexagonal wurtzite) -Photocatalytic activity (80% for 3h); others it's good	[9], [10], [22], [23], [24], [25], [26], [27], [28]
SnO_2	-Spray pyrolisis -Spin-coating -Dip-coating	-Crystalline phase (cassiterite, rutile, tetragonal) -High refractive index	[29], [30], [31], [32]

	-Hydrothermal method	-Good photocatalytic activity	
Fe_2O_3	-Wet film application	-Good anticorrosion properties	[33]
$TiO_2 - SiO_2$	-Sol-gel synthesis (powder) -Dip-coating	-Crystalline phase (anatase in amorphous silica matrix and anatase and silica phase, anatase, anatase and rutile) -Good photocatalytic activity (98% in 30 min) -High transmission -Strong superhydrophilicity. -Good scratch properties	[34], [35], [36], [37], [38], [39], [40], [41],
$TiO_2 - ZnO$	-Dip-coating -Auto-ignition -Spin-coating	-Crystalline phase (anatase and zincite, wurtzite) -Photocatalytic activity (20% for 1.6h, good) -Photocatalytic H_2 generation	[9], [10], [42], [43], [44]
$TiO_2 - SnO_2$	-Electrodeposition -Compression -Electrospining -Dip-coating	-Crystalline phase (hexagonal titanium, tetragonal tin and, tetragonal SnO_2, anatase and rutile, rutile and cassiterite). -Good photocatalytic activity	[45], [46], [47], [48], [49], [50]
$TiO_2 - Fe_2O_3$	-Hydrothermal methods -Dip-coating	-Crystalline phase (Ti and Fe, anatase, $Fe_2Ti_3O_9$, Ti_3O_5 and Fe_3O_4, anatase and	[51], [52], [53],[54], [55]

		hematite).	
		-Good photocatalytic activity (visible light)	
$SiO_2 - ZnO$	-Precipitation method - Sol-gel synthesis (powder) -Slip-casting -Dip-coating -Bath deposition	-Crystalline phase (zincite, wurtzite, -Good photocatalytic activity (MO with 40% ZnO the best)	[56], [57], [58], [59], [60]
$SiO_2 - SnO_2$	-Dip-coating -Inverse dip-coating, powder in tube. - Sol-gel synthesis (powder) -Electrospinning -Hydrothermal process	-Refractive properties. -Crystalline phase (rutile in SiO_2 amorphous phase, cassiterite, tetragonal SnO_2 and amorphous SiO_2, SnO_2 rutile (less 25% SiO_2)) -Photocatalytic activity (better with SiO_2)	[61], [62], [63], [64], [65]
$SiO_2 - Fe_2O_3$	-Chemical liquid deposition -Spray pyrolysis -Hydrothermal method -Annealing	-Crystalline phase (metallic aluminium, amorphous silica, hematite, amorphous silica with nanometric crystallization Fe_2O_3) -Supermagnetic properties	[66], [67], [68], [69]
$ZnO - SnO_2$	-Pulsed laser deposition -Screen printing	-Crystalline phase (SnO_2, ZnO hexagonal wurtzite and SnO_2 tetragonal, cassiterite tetragonal, hexagonal and orthorhombic	[70], [71], [72], [73], [74], [75]

	-Powders -Dip-coating -Spin-coating and spray pyrolysis	ZnO and SnO_2) -Good optical properties -Photocatalytic activity (together better)	
$ZnO - Fe_2O_3$	-Photochemical deposition -Precipitation	-Crystalline phase (hexagonal wurtzite and Fe_2O_3, -Good photocatalytic activity	[76], [77]
$TiO_2 - SiO_2 - ZnO$	-Precipitation	-Crystalline phase (hexagonal phase of Zn and 3 component phase) -Photocatalytic activity	[22]
$TiO_2 - SiO_2 - SnO_2$	-Spin-coating -Electrospinning	-Crystalline phase (anatase, tetragonal TiO_2) -Photocatalytic activity -Superhydrophilicity (self-cleaning effect) under UV.	[78], [79]
$TiO_2 - SiO_2 - Fe_2O_3$	-Dip-coating	-Crystalline phase (Fe_2O_3 with TiO_2 and SiO_2 amorphous, anatase) -Photocatalytic activity (Fe_2O_3 increases the absorption of UV)	[80], [81]
$TiO_2 - SiO_2 - ZnO - SnO_2$	-Electrospinning	-Crystalline phase (tetragonal TiO_2, cubic SnO_2, hexagonal ZnO and amorphous SiO_2)	[82]

1.2.1. Titanium (IV) ethoxide (TiEt)

Titanium (IV) ethoxide (Fig.1) is used widely as a precursor for the synthesis of Ti^{4+} ions, to obtain titanium dioxide.
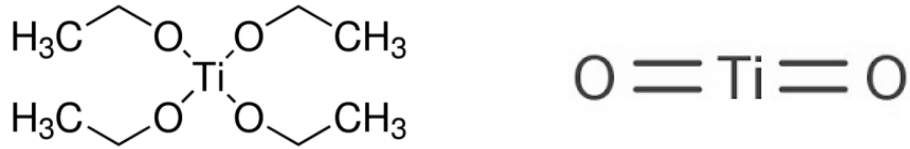

Figure 1. Titanium (IV) ethoxide (left) and titanium dioxide (right) structure.

Titanium dioxide is one of the most important semiconductors and plays a most promising role in several areas because of its high photocatalytic activity, high refractive index, resistance to corrosion, and absence of toxicity, low cost and excellent chemical stability under various conditions.

For these properties, titanium dioxide has attracted significant attention of researchers because it shows the most promising prospect in environmental purification as the photocatalytic degradation of pollutant, photoelectrochemical solar energy conversion, dye sensitized solar cells, gas sensor, hydrogen by water photoelectrolysis and optical coating application. [6] [10] [36] [83]

Titanium dioxide gels can be obtained when the hydrolysis of titanium alkoxides is performed in presence of glacial acetic acid. This carboxylic acid does not act only as an acid catalyst, but also as a ligand and changes the alkoxide precursor at a molecular level therefore modifying the whole hydrolysis condensation reactions. [8] [84]

1.2.2. Tetraethyl ortosilicate (TEOS)

Tetraethyl ortosilicate (Fig.2) is used as a precursor to obtain silica.
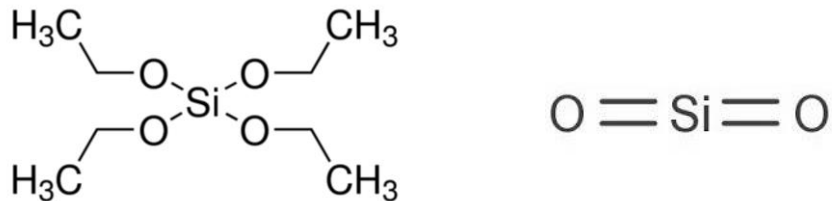

Figure 2. Tetraethyl ortosilicate (left) and silica (right) structure.

Silica gels are low-density, high porosity materials and possess desirable physical properties, such as extremely low thermal conductivity, high acoustic impedance, large specific surface area and low relative dielectric constants. Because of these remarkable properties, experimental and theoretical investigations are mostly focused on silicon compounds and these gels are ideal for various applications, such as thermal super insulators, adsorbents, sensors, catalyst carriers and inorganic fillers. [85] [86]

Also, silica is widely used in optical applications, such as antireflective coatings, high reflecting, mirrors and hydrophilic coating, because of its low cost and it is a material with high chemical, thermal and mechanical stabilities. [36]

1.2.3. Zinc acetate (ZnAc)

Zinc acetate (Fig. 3) is the precursor of the zinc oxide.

Zinc oxide has become an interesting metal oxide because of its properties, it is a semiconductor with a wide band gap (3.3 eV), which exhibits a hexagonal wurtzite structure; also it has large excitation binding energy, it is abundant in nature and environmentally friendly. [87] [88]
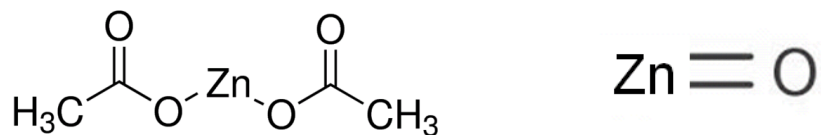

Figure 3. Zinc acetate (left) and zinc oxide (right) structure.

For these properties, zinc oxide films have been studied extensively and are used in many applications such as solar cells, gas sensors, transparent conductive electrodes, display units, varistors, piezoelectric transducers, optical waveguides, etc. [9] [23]

1.2.4. Tin (IV) chloride pentahydrate (SnCl4)

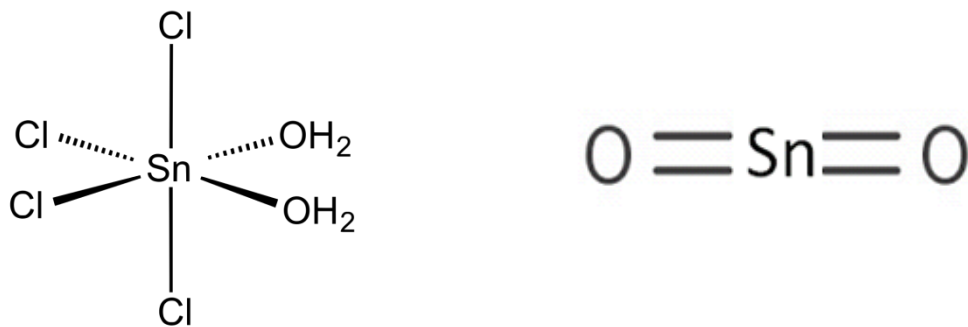Tin (IV) chloride pentahydrate is the precursor of tin dioxide (Fig.4).

Figure 4. Tin (IV) chloride pentahydrate (left) and tin dioxide (right) structure.

Tin dioxide is a semiconductor with a wide band gap (3.5- 4 eV) having a refractive index of approximately 2.0 and a tetragonal crystal structure. Due to its unique physical properties such as high electrical conductivity, high transparency in the visible part of the spectrum and high reflectivity in the IR region is used in optoelectronic devices, hybrid microelectronics and solar energy applications, such as liquid crystal displays, electro chromic and electroluminescent cells and photovoltaic devices. Also it is stable up to high temperatures, have excellent resistance to strong acids and bases and they have very good adhesion to many substrates. [89] [90]

1.2.5. Iron (II) acetate (FeAc)

Iron (II) acetate is the precursor of iron (III) oxide (Fig. 5).
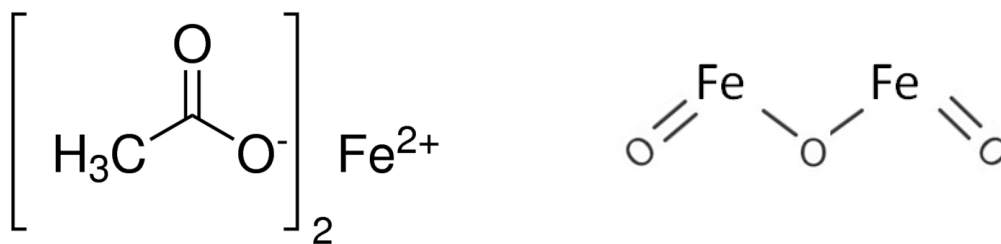

Figure 5. Iron (II) acetate (left) and iron (III) oxide (right) structure.

Iron oxide has applications in numerous fields, such as photoelectrodes, gas sensing, catalysis, magnetic recording and medical fields, photoelectrochemical solar cells and rechargeable batteries. It is also required for water electrolysis in the presence of sunlight. [91]

1.2.6. Dietalonamine (DEA)

Diethanolamine (Fig.6) is an amino alcohol commonly used in the preparation of soaps and surfactants, agricultural chemicals and in the textile processing. It is used as an absorbent for capturing CO_2. Also, its toxic and carcinogenic effect has been studied. [92]
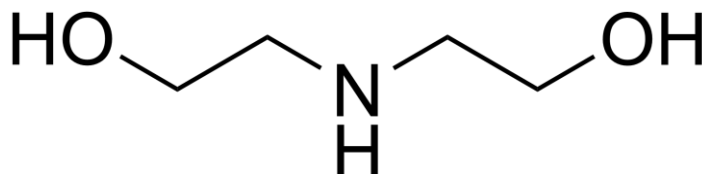

Figure 6. Diethanolamine structure.

Moreover, DEA is usually used as a solvent and stabilizer in common sol-gel processing. In this project is used in the ZnO sol-gel to easy the suspension of the zinc acetate in ethanol. [26] [27] [28] [93] [94] [95]

1.2.7. Surfactants

Surfactants are surface active agents which reduce the tension between two immiscible systems, as well as the interaction of forces between various fluid systems or between a liquid and solid phase. They are composed of hydrophobic and hydrophilic groups and are divided in four classes, depending on their hydrophilic groups. [97]

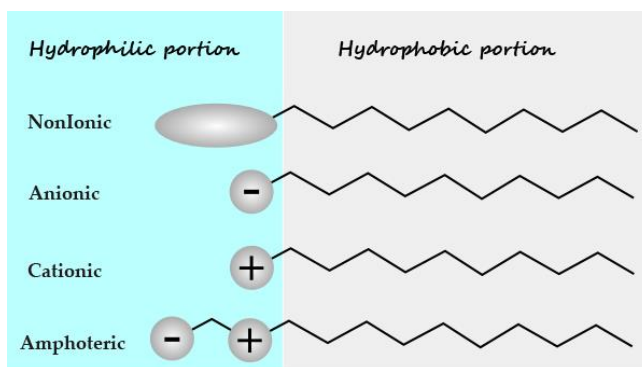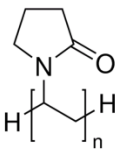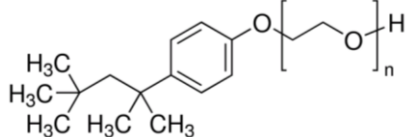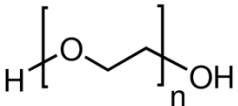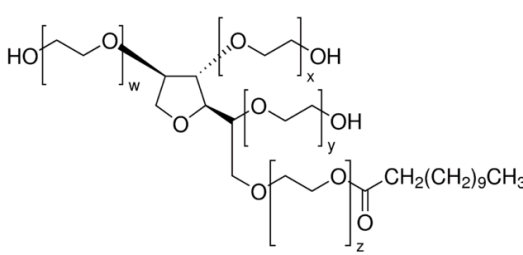The different classes (Fig. 7) are explained below:

Figure 7. Different types of surfactant structure [115]

- Non-ionic: No formation of ions in aqueous solution; the hydrophilic part are OH-groups, ethylene oxide or propylene oxide chains. (Ex: Tritons X-100, Pluronic F-127, Polyvinilpyrrolidone, Polietilenglicol, etc.).

- Anionic: Negatively charged in aqueous solution, very often sulfonate, sulphate or phosphate groups. (Ex: Sodium dodecyl sulphate, Sodium dodecyl sulfonate, etc.).

- Cationic: Positively charged in aqueous solution, the main components being quaternary ammonium compounds. (Ex: Cetyltrimethylammonium bromide, Hexadecyltrimethylammonium bromide, etc.).

- Amphoteric: Contain both anionic and cationic parts in the same molecule which cannot be separated by dissociation. (Ex: AMA L770, N-(2-carboxyethyl) N-2-ethylhexyl) monosodium salt, etc.).

There are some studios about the influence of the different surfactants in the precursors that are used in this project (Table 2). The size, structure, crystallinity and to some extent the morphology of the precursors are dependent on the nature of surfactants.

Table 2. Most common used types of surfactants.

Types of surfactants	Surfactant	Structure
Non-ionic	Polyvinilpyrrolidone (PVP)	
	Polyethylene glycol tert-octylphenil ether (Triton X-100)	
	Polyethylenglycol (PEG)	

	Pluronic F-127	
	Polyethylene glycol sorbitan monolaurate (Tween 20)	
Cationic	Dodecyltrimethylammonium bromide (DTAB)	
	Hexadecyltrimethylammonium bromide (CTAB)	
	Myristyltrimethylammonium bromide (TTAB)	
Anionic	Sodium dodecyl sulphate (SDS)	

In the case of titanium dioxide, some research [98] establish that adding surfactants (in the optimal content 1.5wt %) to the solution it is beneficial to reducing the aggregation of particles; however the effect of cationic surfactants is not as good as anionic surfactants. Others [100] [101], show that using non-ionic surfactants (PVP, Triton X-100, PEG and Pluronic F-127) the samples have smaller grain size resulting a large surface area, high pore volume, also they have a higher photocatalytic activity. Also, some of them establish [102] that using surfactants (cetyltrimehyl ammonium bromide and urea) and increasing temperature the morphology is polycrystalline.

There are researches about how different classes of surfactants (DTAB- cationic, SDS-anionic and Tween 20-nonioinic) affect silica coatings [103]. The results show that the roughness and optical properties (λ_{max} (nm)) are in this order SDS>DTAB>Tween 20.

Thermal stability of Tween 20 is probably high is comparison to DTAB. The contact angle data shows that the wettability properties of the film are controlled by roughness, and the film with Tween 20 surfactant shows least contact angle in comparison to DTAB and SDS. This infers that Tween 20 promotes nice spreading of sol, as the cohesive forces are reduces to a level where form the materials developed the uniform thin film. Hence, by controlling the surface structure of the film, efficiency of anti-wetting, self-cleaning, anti-abrasion, and anti-rusting properties of thin film will be enhanced.

Also, the zinc oxide is affected by surfactants [104] [105] [106]. It has been shown that using PEG 400 not only significantly shortens the reaction time for preparing ZnO, but also increases the crystallinity. Also, it can be established that with non-ionic surfactants (Triton and PEG) a larger crystalline size is obtained than with anionic (SDBS and SDS) and cationic surfactants (CTAB). The crystal grown show smaller average size when it is used the CTAB. And in relation with optical properties, a significant blue shift in the excitonic absorption for materials prepared in the presence of anionic and cationic surfactants.

The effect of surfactants in the tin dioxide material has been studied too. Some research [107] establish that anionic surfactant (SDS) and cationic surfactants (CTAB) at the suitable addition amounts can largely influence the morphologies of tin dioxide nanocrystals (size increases from 1.75 to 4.2 nm). Although, the non-ionic surfactant (PVP) change the morphologies, the impacts are less obvious. However, other research [108] [42] establish that cationic surfactant (CTAB) assisted tin dioxide nanoparticles are the best, in terms of size, morphology, structure and optical properties.

Finally, the iron oxide is also affected by surfactants, however there are less researches. One of them about cationic (CTAB, OTAB, TTAB) and non-ionic (PEG, Triton X-100 and Pluronic F127) [109], establish that PEG and F127 produces smoother surface and lower photocurrent. The three cationic surfactants have better photocatalytic activity than the three non-ionic surfactants and they have the highest current sensitivity, lowest band gap and highest absorption.

1.3. SOL-GEL DEPOSITIONS METHODS

Sol-gel processing is widely used in the synthesis of inorganic and organic-inorganic hybrid materials and capable of producing nanoparticles, nanorods, thin films and monolith.

Prior to sol-gel transition or gelation, sol is diluted in a suspension in a solvent and typically sol-gel films are made by coating sols onto substrates. Although, a lot of methods are available for applying liquid coatings to substrates, the choice depends on solution viscosity, desired coatings thickness and coating speed. [110]

Basically, thin-film deposition technologies are either purely physical, such as evaporative methods, or purely chemical, such as gas- and liquid-phase chemical processes. A considerable number of processes that are based on glow discharges and reactive sputtering combine both physical and chemical reactions. A classification scheme is presented in Table 3. [111]

Table 3. Classification of deposition methods

Evaporation methods	Vacuum evaporation: - Conventional - Electron-beam evaporation - Molecular-beam epitaxy (MBE) - Reactive Evaporation	
Glow-discharge processes	*Sputtering:* - Diode sputtering - Reactive sputtering - Bias sputtering (ion plating) - Magnetron sputtering - Ion beam deposition - Ion beam sputter deposition - Reactive ion plating - Cluster beam deposition (CBD)	*Plasma processes:* - Plasma-enhanced CVD - Plasma oxidation - Plasma anodizaion - Plasma polymerization - Plasma nitridation - Plasma reduction - Microwave ECR plasma CVD - Cathodic arc deposition

Gas-phase chemical processes	*Chemical vapour deposition (CVD):* - Epitaxial CVD - Atmospheric-pressure CVD - Low-pressure CVD - Metalorganic CVD - Photo-enhanced CVD - Laser-induced CVD - Electron-enhanced CVD	*Thermal forming processes:* - Thermal oxidation - Thermal nitridation - Thermal polymerization - Ion implantation
Liquid-phase chemical techniques	*Electro processes:* - Electroplating - Electroless plating - Electrolytic anodization - Chemical reduction plating - Chemical displacement plating	*Mechanical Techniques:* - Spray pyrolysis - Spray-on techniques - Spin-on techniques - Dip-coating

The most commonly used methods for sol-gel film deposition are spin-coating and dip-coating within of *Mechanical techniques*. [110]

1.3.1. Dip-coating

Dip-coating is based in an immersion of a substrate in a solution and withdrawn at a constant speed. There are two types of dip-coating. The batch (Fig. 8) one is divided in five stages: immersion, start-up, deposition, drainage and evaporation; however the continuous dip-coating process (Fig. 9) is simpler because it separates immersion from the other stage, essentially eliminates start-up and "hides" drainage in the deposited film.
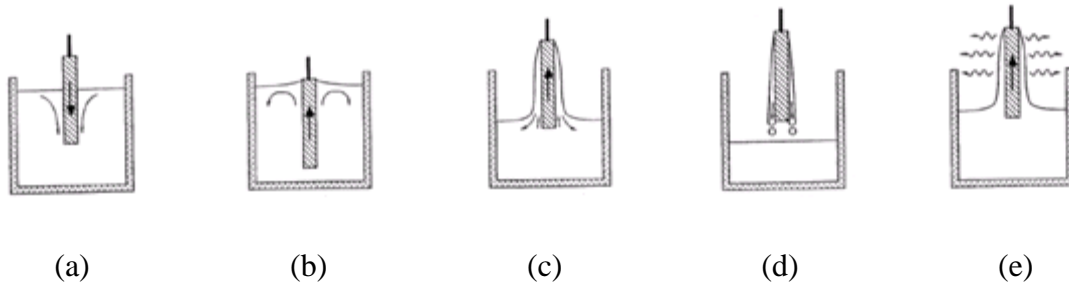
Figure 8. Bach dip-coating stages: (a) Immersion, (b) Start-up, (c) Depositions and drainage, (d) Drainage, (e) Evaporation. [3]
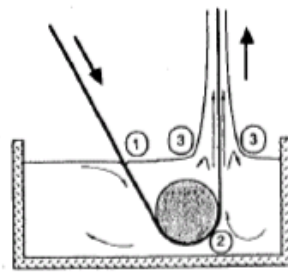
Figure 9. Continuous dip-coating process. [3]

The thickness of the deposited film is related to the position of the streamline dividing the upward and downward moving layers. There are as many as six forces that govern the film thickness and position of the streamline:

- Viscous drag upward on the liquid by the moving substrate.

- Force of gravity.

- Resultant force of surface tension in the concavely curved meniscus.

- Inertial force of the boundary layer liquid arriving at the deposition region.

- Surface tension gradient.

- Disjoining or conjoining pressure. [3]

When the liquid viscosity (η) and substrate sped (U) are high enough to hold the meniscus curvature, the thickness (h) is governed by a balance between the viscous drag ($\eta U / h$) and gravity force (proportional to h, where ρ is the density of the liquid and g is the acceleration due to gravity). Thus

$$h = c_1 \left(\frac{\eta\, U}{\rho\, g}\right)^{1/2} \qquad (1)$$

Where the constant of proportionality c_1 is ~0.8 for Newtonian liquids.

When the liquid viscosity and substrate speed are not high enough, the balance of forces is modulated by the ratio of viscous drag to the liquid-vapour surface tension γ_{LV}, according to the following equation derived by Landau and Levich: [112]

$$h = 0.944 \left(\frac{\eta\, U}{\gamma_{LV}}\right)^{1/6} \left(\frac{\eta\, U}{\rho\, g}\right)^{1/2} \qquad (2)$$

However, in the equations not take into account the evaporation of solvent and the continuous condensation between nanoclusters dispersed in the sol (Fig. 10), although it can be established that the relationship between the thickness and the coating variables is the same.
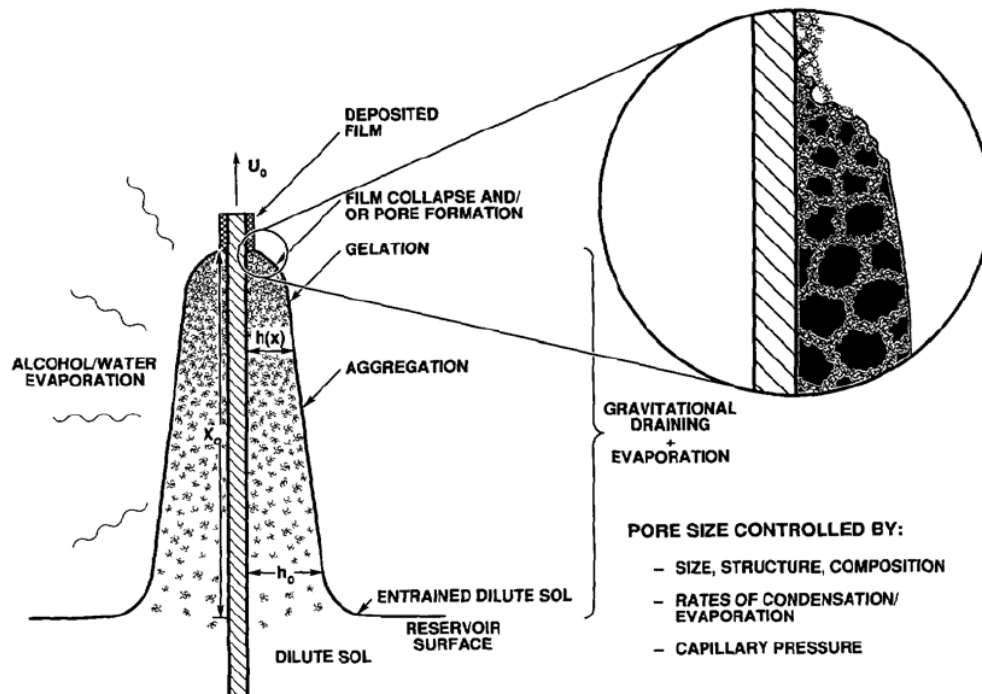

Figure 10. Schematic evaporation process of solvent and continuous condensation during dip-coating. [110]

The thickness of a dip-coated film is commonly in the range of 50-500 nm, though a thinner film of ~8 nm per coating. [110]

1.4.DRYING TECHNIQUE AND SINTERING

After the dip-coating the slides should be dried and then the samples are subjected to heat treatment.

1.4.1. Drying

Drying is a complex process that involves four processes (Fig. 11):

1. *Constant Rate Period*, the evaporation rate per unit area of the drying surface is independent of time (nearly constant), so when the decrease in volume of the gel is equal to the volume of liquid lost evaporation. However, note that gels may also shrink faster than the water can evaporate if rapid cross-linking and syneresis is occurring; in this case the pore size distribution will be strongly influenced by the cross-linking, whereas gels which shrink by evaporation of water from compliant structure will suffer pore collapse.

2. At the *Critical Point*, the gel becomes sufficiently stiff to resist further shrinkage as liquid continues to evaporate and the liquid begins to recede into the porous structure of the gel increasing the tension in the pores and decreasing the vapour pressure of the liquid.

3. *First Falling Rate Period*, the evaporation rate decreases approximately linearly with time and the temperature of the surface rises above the wet-bulb temperature. So it is when the liquid flow through partially empty pores. As these empty, the vapour pressure decreases with increased capillary stress. Thus, cracking may occur at any stage in this phase of the drying.

   Most of the evaporation is occurred at the exterior surface, and the surface remains below the ambient temperature. Inhomogeneity can result as the flow carries solutes towards the surface where they may precipitate. At the same time, some liquid evaporates within the unsaturated pores and the vapour is transported by diffusion.

4. *Second Falling Rate Period*, the evaporation rate is difficult to predict as it depends on the pore-size distribution, the relative temperatures of the bulk and surface of the sample, and the possible presence of isolated pockets of liquid at irregular pore surfaces between the main liquid interface within the pores and the outer gel/air

interface. This is the final stage of drying when liquid can escape only by diffusion of its vapour to the surface. [3] [112] [116]
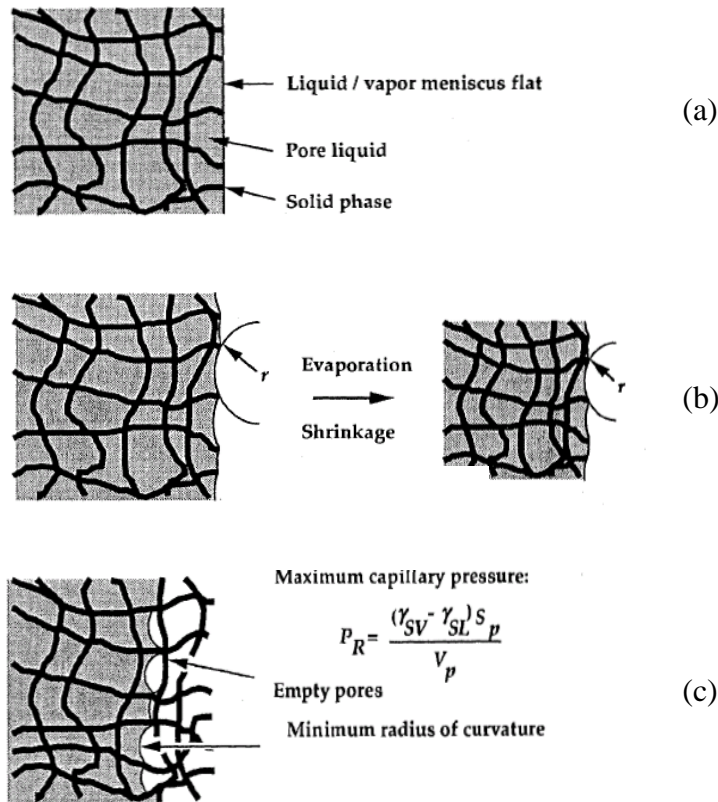
Figure 11. Schematic illustration of drying process. (a) Initial condition. (b) Constant rate period. (c) Falling rate period. **[112]**

The stress and cracking problems may be avoided using different methods as supercritical drying changing water for alcohol and applying high temperature or pressure, freeze-drying, adding additives to control the process, etc.

1.4.2. Sintering

Sintering is the process of compacting and forming a solid mass of material by heat or pressure without melting it to the point of liquefaction. The atoms in the materials diffuse across the boundaries of the particles, fusing the particles together and creating one solid piece.

Although the silica gels prepared and dried at or near room temperature have many applications, heat treatment is necessary for the production of dense glasses and ceramics

from gels. However, the detailed effects of heat treatment depend on the particular characteristics of the material at the end of the low-temperature drying process.

The theoretical analyses and experimental studies have produced an excellent qualitative understanding of sintering in terms of the driving forces, the mechanisms, and the influence of the principal processing variables such as particle size, temperature, applied pressure and gaseous atmosphere. [112] [116]

1.5.SOL-GEL SYSTEMS

1.5.1. TiO$_2$-SiO$_2$ sol-gel coatings

Some authors have obtained the transparent uniform titania-silica composites thin films by dip-coating [36] [37] [38] and spin-coating [40] on a substrate, after getting a sol-gel with these components. In the sol-gel preparation the four authors obtain the sol-gel mixing the precursors with ethanol.

Both, TiO$_2$ and SiO$_2$ are typical optical thin films with high transparency and low absorption in visible and near infrared regions. Furthermore, as they are low cost, safe and abundant materials with high chemical, thermal and mechanical stabilities, they have been widely used for various optical applications, such as antireflective coatings, high reflecting, mirrors or hydrophilic coating. The coatings with high hydrophilic properties have many advantages, such as, sterilization, deodorization, antipollution, self-cleaning, etc. Moreover, transparent TiO$_2$-SiO$_2$ films on glass could form the basis for self-cleaning of indoor windows, lamps or windshields.

In relation to these applications, the authors want to improve different properties. The aim of *Liyun Chen* and co-researcher (2016) [36] was to investigate the influence of the composition nanocomposite TiO$_2$-SiO$_2$ thin films on their microstructure, hydrophilic property and gloss property. The results of their studios establish that the crystal structure depends on the heating temperature; the mainly crystal of titanium dioxide film is anatase when the heat treatment temperature is 200ºC and 400ºC and there is no X-ray diffraction peak of rutile; however it is shown that, when the treatment temperature is 700ºC, the mainly diffraction peak is rutile. Therefore, the results show that doping of SiO$_2$ restrained growth of the grains and promoted forming of nano-particles. On the other

hand, the hydrophilic property of the coating increases by heating and the gloss property of the coating surface can be greatly increased after the enamel coated with TiO_2-SiO_2 film.

In the *Najme Iari* and co-researchers work (2015) [37], multilayer film structures were fabricated to improve antireflective properties. The results show a high transmission about 99% and the multilayer coatings are more compact than single ones, this property causes more reductions surface reactivity and minimizes the absorption of both moisture and airborne contaminants in the pores, furthermore it makes the multilayer coatings more durable.

Moreover the purpose of *A. Shokuhfar* and co-researchers (2012) [38] and *Sanjay S.Latthe* (2014) [40] were to experimentally assess the SiO_2-TiO_2 films to benefit the self-cleaning application. These researches prove that annealing temperature is an important parameter; the particle size increases from 19 to 42 nm by increasing the annealing temperature from 500ºC to 700ºC, and the films are crack-free at 500ºC. X-ray analysis shows the crystal anatase and rutile as main phases annealed at 500ºC and 700ºC, respectively. Films annealed at temperatures below 100ºC are not adhesive, do not adhere well to the glass substrate, and flake off into the solution. Annealing at 200ºC produces a film that can be removed from the surface by soft scratching. Films annealed at 500ºC are adherent. Annealing at 700ºC is not suitable and practical, because at this temperature glass substrate begins to soften and lucidity reduced. Linked to photocatalytic activity, it decreases if the heat treatment temperature from 500ºC to 700ºC. This can be assumed to result from the increasing conversion from anatase into rutile.

Other authors [39], [34], [35], after sol-gel synthesis obtain powders for different studios. In recent years, titania-silica composites are very promising in field of heterogeneous photocatalysis, since they could provide simultaneously enhanced photocatalytic and thermal properties compared to pure TiO_2 photocatalyst. These compounds are used in oxidation of organic pollutants in water, SiO_2 is a good medium, which not only facilitates adsorbing organics and transfers those adsorbed compounds to active sites on TiO_2, but also benefits to the dispersion of the TiO_2 particles.

Magali Bonne and co-researchers (2010) [35] establish that in the nanocomposites, the titania nanodomain size remains limited, and no important pore plugging can be evidenced when treated at low/intermediate temperature (400ºC). Due to the limited TiO_2 cluster size, high surface area (450 $m^2 \cdot g^{-1}$) can be maintained. Also, the surface and pore volume of the nanocomposites decreases while increasing calcinations temperature from 400ºC to 800ºC, however a high thermal stability is obtained with a limited crystal growth while increasing the calcinations temperature up to 800ºC.

Moreover, *Abdolreza Nilchi* and co-researchers (2011) [35], show with XRD that the TiO_2-SiO_2 nanocomposites has crystalline anatase phase in amorphous silica matrix, the TEM images show that the nanoparticles size is between 5-9 nm and the specific surface area decreases when calcinations temperature increases (reached 142.38 m^2 g^{-1}). Significantly, such as increase in the surface area and the existence of tetrahedrally coordinated TiO_2, improves the photocatalytic activities of the TiO_2-SiO_2 ceramic. The same way *Shaozheng Hu* and co-researchers (2012) [39] establish that all samples are mixture of anatase and rutile phases and therefore they have good photocatalytic activity.

1.5.2. TiO$_2$-SiO$_2$-ZnO sol-gel coatings

ZnO has received considerable attention in various areas such as catalysis, systems, drug delivery and targeting, anti bacterial, cancer therapy and enzyme immobilization, due to its low toxicity, good biocompatibility, tunable properties and excellent chemical stability. In the *B. Kaleji* and co-researchers work (2015) [22] ZnO nanoparticles and ZnO-TiO_2-SiO_2 nanocomposites are synthesized by a simple sol-gel method. For preparation of different nanocomposites various amounts of three components are mixed and are heat treated.

Regarding the results, the X-ray pattern show three phases of ZnO, TiO_2 and SiO_2, the SEM images show particles with a average diameter of 100 nm and the effect of temperature on the morphology of the product is investigated, at lower temperature at 400ºC bigger products are obtained and also at 600ºC particles with average particle size of 90 nm are achieved that are higher than product synthesized at 500ºC. Finally, the results of degradation of methyl blue are promising materials with suitable performance in photocatalytic applications.

1.5.3. TiO$_2$-SiO$_2$-SnO$_2$ sol-gel coatings

There are some literature about this system, *Lek Sikong* and co-researcher (2010) [78] obtain SiO$_2$ and SnO$_2$ co-doped TiO$_2$ nano-compostie thin films prepared by sol-gel method to know the effects of film thickness and amount of different precursors in the crystallite size, photocatalytic reaction and hydrophilicity.

According to the results, the thickness of triple-coating layer (238 nm) seems to provide the highest photocatalyitic activity, in contrast to single-coating (54 nm) and double-coating (124 nm). It is apparently that the film thickness has an effect on the photocatalytic activity; photocatalyitic reactions increases with an increase in film thickness due to higher photo-induced electron density transferred from the surface of TiO$_2$. Moreover, the crystallinity of anatase phase, crystallite size and photocatalytic reactions of films decrease with increase in SiO$_2$ content, because it inhibit grain growth and the formation of anatase phase, especially when it synthesized at temperatures less than 600ºC.

Other authors, like *Chao Song* and *Xiangting Dong* (2012) [79], synthesize the fibers of these materials by heating the precursor composite fibers at 800ºC and 900ºC for 8h, after electrospinning. Result show that the precursor composite fibers are amorphous in structure and pure phase. TG-DTA and FTIR reveal that the formation of composite is largely influenced by calcinations temperatures. SEM micrographs indicate that the surface of the precursor composite fibers is smooth and become coarse with the increase of calcinations temperatures. EDS analysis results reveal that the composite nanofibers are only composed of Ti, Sn, Si and O elements

1.5.4. TiO$_2$-SiO$_2$-Fe$_2$O$_3$ sol-gel coatings

There are some literature about these materials separately, however there are not a lot about all together. One of these researches is done by *Hongtao Cui* and co-researchers [80] (2011), the TiO$_2$-SiO$_2$-Fe$_2$O$_3$ films are prepared through an epoxide sol-gel route and dip-coating at room temperature by doping of a little amount of Fe$_2$O$_3$ nanoparticles.

Nanosized Fe$_2$O$_3$ has shown extensive uses in the areas of ferrofluid, gas sensor, magnetic refrigeration, information storage, drug delivery, magnetic resonance imaging,

catalyst and magneto-optic. Also, it exhibits very strong absorptions in the UV range, which indicates its potential applications in the UV absorption coating. However, the strong brown coloration of Fe_2O_3 lowers the transparency greatly in the visible range.

The obtained films show advantages such as high stability, efficient absorption in the UV region, high transparency in the visible range and very low oxidation catalytic activity due to the intrinsic non oxidation property of the amorphous TiO_2 and Fe_2O_3. Moreover, it is found that 2.3 nm Fe_2O_3 nanoparticles doped films exhibit stronger UV absorption than the films doped with 5.1 nm particles because of the increased grain strain of the nanoparticles with smaller size.

2. METODOLOGICAL PART

In this project five different systems are studied. In previous sections, it has shown the precursors that have been used to obtain the final materials. In a methodological part it is necessary to describe the sol compositions, preparation technique for the microscope slides before coatings, the dip-coating technique using different rates, drying, sintering process of the final material and the methods of investigations of the final material.

2.1. SOL PREPARATION

The first step to obtain the final material is the sol preparation. The sols studied in the present work were prepared with different compositions that are shown below in Table 4:

Table 4. Chemical composition ranges of the sol–gel films of different systems.

Precursor / Systems	Sol	TiEt	TEOS	ZnAc	SnCl₄	FeAc
$TiO_2 - SiO_2 - ZnO$	VC_z	50	30	20	-	-
$TiO_2 - SiO_2 - SnO_2$	VC_s	50	30	-	20	-
$TiO_2 - SiO_2 - Fe_2O_3$	VC_f	50	30	-	-	20
$TiO_2 - SiO_2 - ZnO - SnO_2$	VC_4	50	30	10	10	-
$TiO_2 - SiO_2 - ZnO - SnO_2 - Fe_2O_3$	VC_5	50	30	10	5	5

Titanium (IV) ethoxide, tetraethyl ortosilicate (TEOS), tin (IV) chloride pentahydrate, zinc acetate and iron (II) acetate, ethyl alcohol, glacial acid and diethanolamine were used to prepare sols for development dip-coatings. In all of them was used ethanol as a solvent, with a molar ratio 1:10.

The procedures of each sol preparation sequence are explained below.

2.1.1. Preparation of TiO₂ sol (A)

The titanium dioxide sol was obtained using titanium (IV) ethoxide precursor. First, it was mixed with glacial acetic acid, with a titanium (IV) ethoxide: glacial acetic acid molar ratio 1:4 [17] the acetic acid is not only used as a catalyst, also is used for control hydrolysis and condensation reactions, because it reduces the availability of groups that hydrolyse and condense easily through the formation of a stable complex. [84]

The titanium (IV) ethoxide and glacial acetic acid were maintained in stirring for one hour.
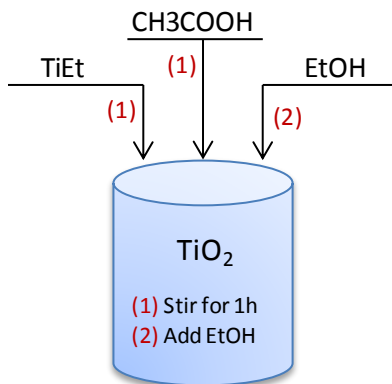

Figure 12. Preparation of TiO$_2$ sol.

2.1.2. Preparation of SiO$_2$ sol (B)

The silica dioxide was obtained by mixing tetraethyl ortosilicate with ethanol and maintained them in stirring, like TiO$_2$ sol, for one hour. After one our sol A was added to sol B.
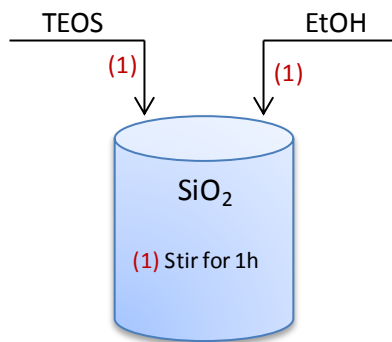

Figure 13. Preparation of SiO2 sol.

2.1.3. Preparation of ZnO sol (C)

Zinc acetate was used as a precursor in order to obtain zinc oxide. It was mixed with ethanol; however, it could not dissolve very well, so diethanolamine (DEA) was added to dilute this solution.

In literature appears different quantities of DEA, in some of them [26], [93], [27], [28], is needed a lot of quantity of ethanol to dissolve Zn acetate and get transparent sol, in some

cases [26] it is not enough ethanol. For this reason, the quantity of DEA was chosen that appears in [95] - 1:1 Zinc acetate: DEA as a molar ratio.

This suspension was maintained in stirring for 20 minutes, then it was applied 4 minutes of ultrasounds at 60 Hz in continue mode.
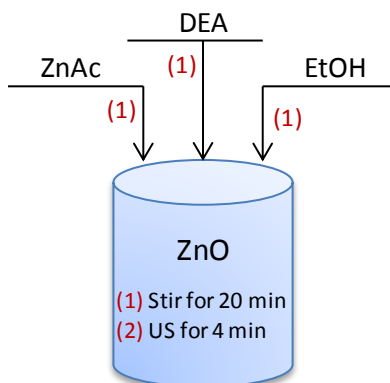

Figure 14. Preparation of ZnO sol.

2.1.4. Preparation of SnO₂ sol (D)

The tin oxide was obtained like the other sols, mixing with ethanol the exact quantity of tin (IV) chloride pentahydrate. The suspension was stirred for 20 minutes.

Figure 15. Preparation of SnO₂ sol.

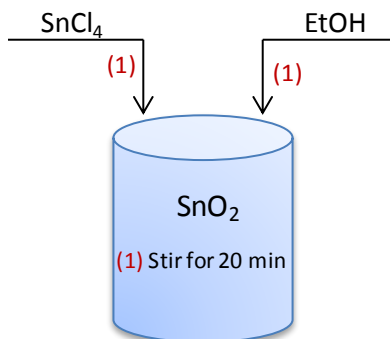## 2.1.5. Preparation of Fe₂O₃ sol (E)

The iron (III) oxide was obtained with iron (II) acetate as a precursor and ethanol. The same way that zinc acetate, iron (II) acetate did not dissolve very well, for this reason, it was necessary to apply ultrasound. The procedure was the same that the zinc oxide sol; stirred for 20 minutes, applied the ultrasound at 60 Hz in continue mode for 4 minutes.

35
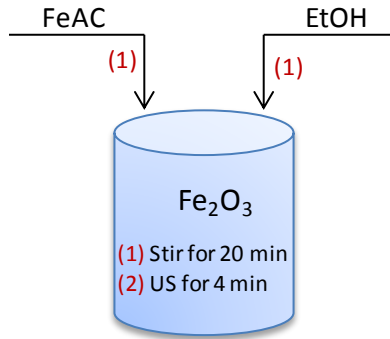
Figure 16. Preparation of Iron (III) oxide sol.

2.1.6. Preparation of three, four and five components sol.

Once all sols was obtained separately the three, four or five components were obtained adding the sols in a determinate order; to do the three components sols it was added the (A) sol to the (B) and then add (C), (D) or (E). And for the four and five components was like three components, but adding firstly (C), secondly (D) and (E) at the end. After putting together every sols in a glass was necessary stir for 5 minutes more. The Figure 17 shows a scheme of the complete process.

Figure 17. Scheme of the sol-gel process.

2.2. PREPARATION TECHNIQUE OF MICROSCOPE SLIDES.

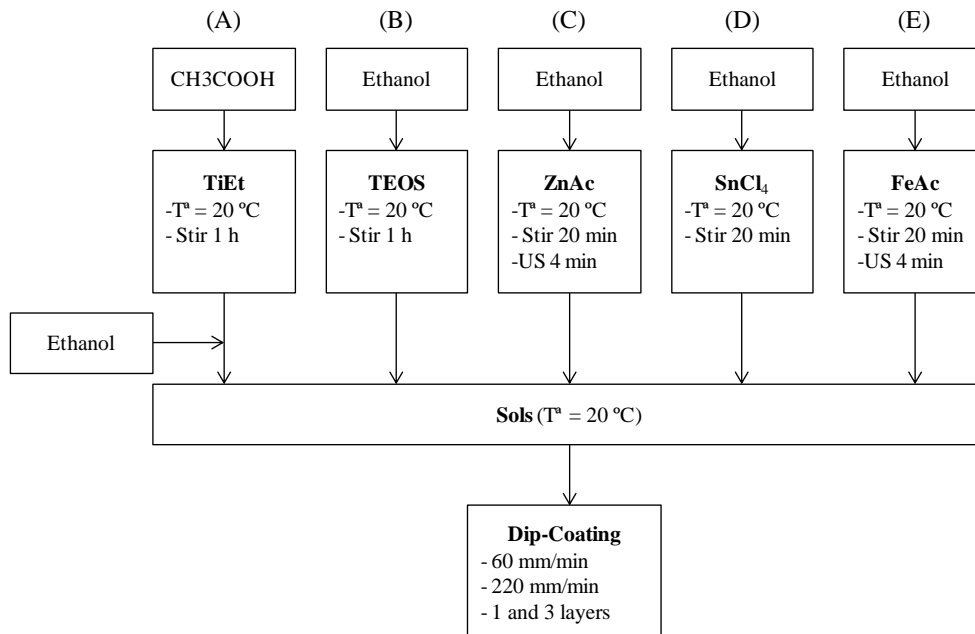Soda-lime silicate glass surface cleaning by mechanic-chemical treatment provided smooth substrate for the deposition of sol-gel film. However, storage of such prepared glass samples at 60 ^{o}C during more than 3-5 hours resulted in corrosion leading almost to the same root mean square roughness as detected for untreated glass. Glass cleaning procedure remarkably influenced the nanostructure of sol-gel films [113]. So, to minimize the unnecessary impurities on the surface the substrates were prepared right before the dip-coating process.

The Menzel-Glaser microscope slides (soda-lime silicate glass substrates) have to be cleaned to remove all mechanical dirt, fingerprints and other impurities from the surface. The cleaning steps were:

1. Washed with water

2. Washed with cerium dioxide (5%) suspension in ethanol using a sponge, and then rinsed with water

3. Washed with dishwashing detergent "Pur" foam with a sponge and rinsed with water

4. Rinsed them with distilled water and soaked for 5 minutes in distilled water

5. Soaked in 1 N nitric acid for 15 minutes

6. Soaked in absolute ethanol for 5 minutes

7. Dried at 60 ºC for 15 minutes

2.3. COATING PREPARATION

Dip-coating technique is a process where the substrate to be coated is immersed in a liquid and then withdrawn with a well-defined speed under controlled temperature and atmospheric conditions. An accurate and uniform coating thickness depends on precise speed control and minimal vibration of the substrate and fluid surface. The coating thickness is mainly defined by the withdrawal speed and the viscosity of the sol [114].

The film deposition was carried out with dip-coating (KN 4002 KSV NIMA Dip Coater Single Vessel System Small) (Fig. 18).
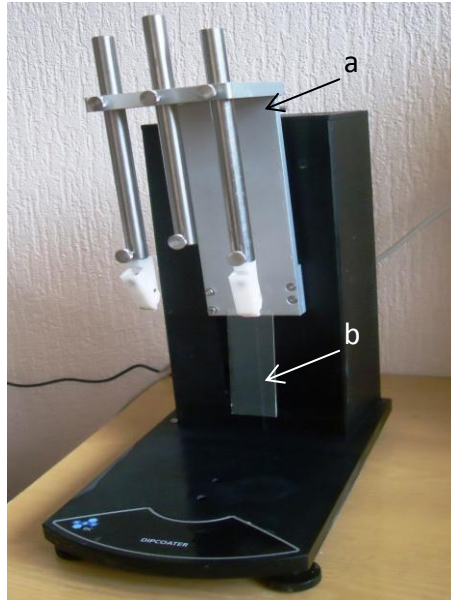
Figure18. Dip-coater KN 4002 KSV NIMA: a) dipping/extraction mechanism.

b) Microscope slide.

All systems that have been explained in the previous section were differ two types of coating at two rates, with one and three layers and slow and fast rates, respectively. The fast rate was fixed in 220 mm/min, the fastest rate that the program allows and the slow rate was fixed in 60 mm/min. Slides were made for each composition, as shown in the following scheme.
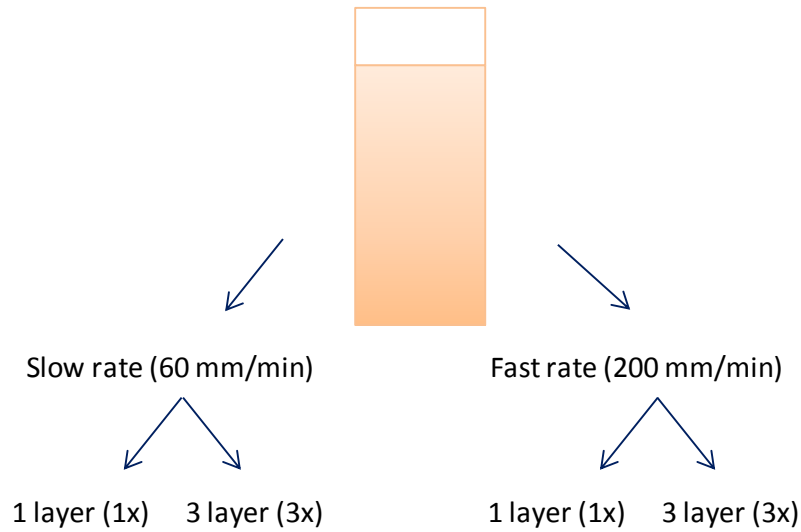
Figure 19. Scheme of coating preparation.

Due to some suspensions (three components with zinc and iron, four and five components) gelled relatively fast (10-20 min) and to keep them homogeneous, the suspensions were stirred between coatings.

2.4.DRYING AND SINTERING

In relation with drying, the substrates were dried at ambient temperature for 5 minutes and at 200ºC for five minutes to dry better and affix the coating after each coating layer applied, then heat treated in furnace at 500ºC for 5 minutes. Finally, once that the slides were dry, it was necessary to do a scratches in the slide coated, before sintering, to measure the thickness.

The sintering process was carried out in the Nabertherm 3000 at 500ºC for 5 minutes; and the rate of heating from room temperature to 500ºC was 5ºC/min. These temperatures were chosen taking literature data [97] and because slides only support till 500ºC. It is known that the glass slides can withstand temperatures up to 560ºC and with higher temperatures; the slides begin to bend and deform. [97]. Figure 20 shows the heat treatment regime previously described.

500ºC for 5 min

5ºC/min

Room temperature   Room temperature
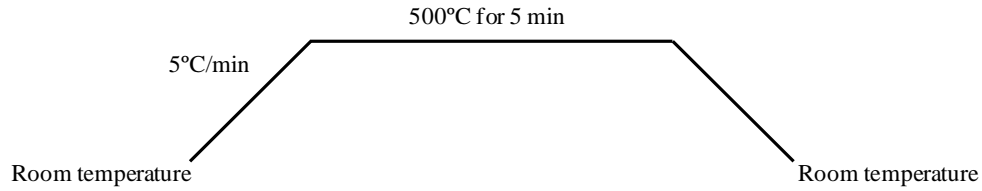
Figure 20. Scheme of heat treatment regime.

2.5. METHODS OF ANALYSIS

To obtain high-quality coatings with suitable properties, it is necessary to analyse curtains parameters of the materials that are obtained with appropriate methods.

In this work it is studied the properties of different sol-gel compositions withTiO_2, SiO_2, ZnO, SnO_2 and Fe_2O_3, different methods used to describe the coatings properties, such as crystal structure, microstructure, phase composition, surface morphology, photocatalytic activity, dimensional topography, etc.

2.5.1. Optical microscopy (OM)

The optical stereomicroscope M 420 (Leica Wild Makroskop) (Fig. 21) and digital Leica DC Camera (magnifications used x100, software Image-Pro Plus 5) was used to visual examination and assessment of the slides before and after sintering, assuring that the coatings does not have any surface defects (cracks, agglomeration etc.).

Figure 21. Optical microscope.

1.1.1. X-ray diffraction (X-ray)

In this project, the phase compositions of the coatings are determined by X-ray analysis (Rigaku Ultima+) using CuKα radiation. A primary use of the technique is the identification and characterization of compounds based on their diffraction pattern.

The method (Fig. 22) is based on constructive interference of monochromatic X-ray and a crystalline sample, where the x-rays are generated by a cathode ray tube, filtered to produce monochromatic radiation, collimated to concentrate and directed towards the sample. The interaction of the incident rays with the sample produces constructive interference (diffracted ray). These diffracted X-rays are then detected, processed and counted providing a unique "fingerprint" of the crystals present in the sample. When properly interpreted, by comparison with standard reference patterns and measurements, this "fingerprint" allows identification of the crystalline form. [125]
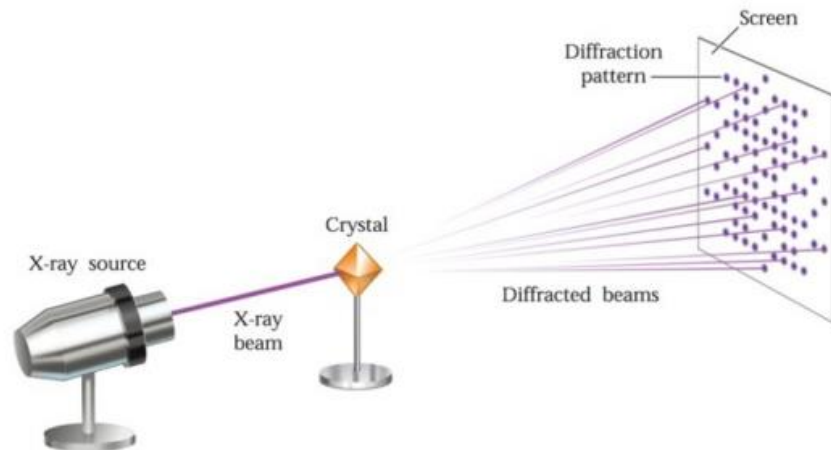

Figure 22. Scheme of X-ray analysis. [Source: Muskingum University web page [126]]

Powders samples before the X-ray analysis were held at 500ºC, finely grounded in an agate mortar and smoothly placed to a sample holder. The prepared samples can be seen in Figure 23. The identification of the phases was performed according to the data of PDF4+ and Sleve+ databases and software Jade 9.
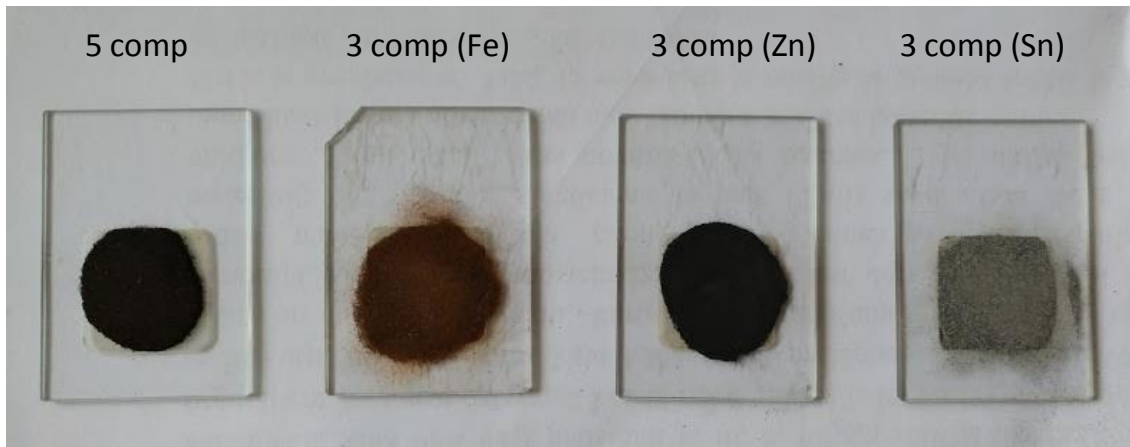
Figure 22. Samples preparation for X-ray analysis

1.1.2. Atomic force microscopy (AFM)

Atomic force microscopy (Fig. 24), unlike traditional microscopes, is a mechanical imaging instrument that measures the three dimensional topography with extremely high resolution, as well as physical properties of a surface by recording the interaction forces between the surface and a sharp tip mounted on a cantilever.

The samples are scanned under the tip using a piezo driven scanning-stage and the topography is displayed as an image. Simultaneously either lateral forces or phase images are acquired. AFM provides spatial information parallel and perpendicular to the surface with nanometric or sub-nanometric range. In addition to topographic high-resolution information, local material properties such as adhesion stiffness can be investigated by analysing the tip-sample interaction forces. [117] [118]
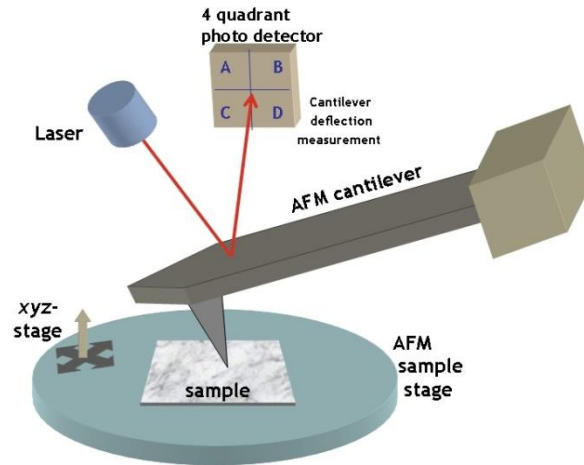
Figure 24. Scheme of AFM microscope. [Source: Physics college [127]]

There are three modes of tip interaction (Fig. 25):

- Contact mode: The sample is scanned in direct contact with the AFM tip. The surface is recorded through deflection of the cantilever.

- Intermittent mode (tapping): The cantilever oscillates at its resonance frequency and is not in constant contact with the sample. When the tip comes close to the surface, sample-tip interactions cause forces to act on the cantilever which alter the oscillation. Thus this mode is particular well suited for delicate samples.

- Non-contact mode: The tip does not contact the sample surface, but oscillates above the adsorbed fluid layer on the surface during scanning.

Figure 25. Modes of AFM. a) contact, b) non-contact, c) tapping. [Source: Slide player [128]]

Therefore, the film morphology and surface structure were investigated by atomic force microscopy (AFM, Veeco SPM II) using non-contact mode. Also, particle size, roughness, surface area, bearing ratio (maximum height that reaches a certain percentage of data points) and thickness were measured using Image Processing v. 2.1 software.

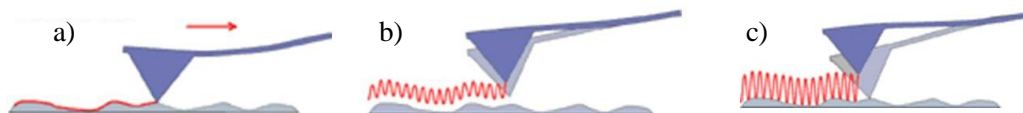The bearing ratio level gives the height value corresponding to a particular percentage on the bearing ratio plot. A bearing ratio plots the percentage of data points that lie above a given height in the height histogram.

The spring constants were 40 N/m and 0.9 N/m. The following parameters were used for the tapping mode: the length of the cantilever - 125 μm the resonant frequency during measurements was 300 kHz. The areas of the samples measured were 50x50, 15x15, 10x10, 5x5 and 1x1 μm^2.

1.1.3. Scanning electron microscopy (SEM)

The scanning electron microscope (SEM) (Fig. 26) uses a focused beam of high-energy electrons to generate a variety of signals at the surface of solid specimens. The signals that derive from electron-sample interactions reveal information about the sample including external morphology (texture), chemical composition, and crystalline structure and orientation of materials making up the sample.

Because the SEM utilizes vacuum conditions and uses electrons to form an image, special preparations must be done to the sample. All water must be removed from the samples because the water would vaporize in the vacuum. All metals are conductive and require no preparation before being used. All non-metals need to be made conductive by covering the sample with a thin layer of conductive material. This is done by using a device called a "sputter coater", using an electric field an argon gas. [119] [120]

The SEM operate by producing electrons at the top of the column, accelerating down and passing through a combination of lenses and apertures to produce a focused beam of electrons which hits the surface of the sample.
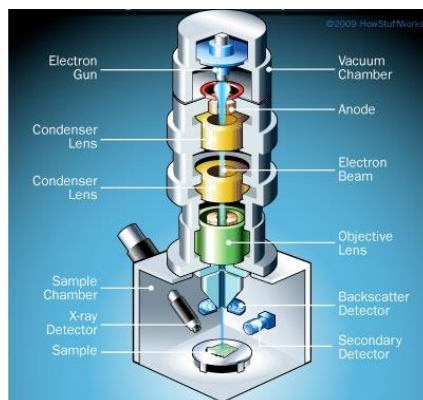
Figure 26. Scheme of SEM microscope. [Source: Science- how stuff works [129]]

The surface morphological character of the coatings was observed by scanning electron microscopy (Fei Nova NanoSEM 650). Samples were cut in approximately 1x1 cm2 pieces and fixed well with the carbon tape to a sample holder. Then, the edges of microscope slides were tinted with the Ag paste to prevent charging of the material as can be seen in Figure 27.

Figure 27. Preparation of samples for SEM.

1.1.4. Photocatalytic properties

The photocatalytic activity of films was evaluated by analysing photocatalytic degradation of methyl orange (MO) in aqueous solution. MO is selected because it is stable under light irradiation and it cannot be photodegraded in the absence of photocatalyst.

To know if the samples have been photodegraded, the transmittance of the solutions samples are monitored by the UV-vis spectrophotometer. UV-vis spectroscopy (Fig. 28) is an absorption spectroscopy technique that involves the absorption of ultraviolet and visible light by a molecule promoting the jump of an electron from a fundamental

molecular orbital to an excited orbital, resulting in transitions of electrons from low energy levels to higher levels. [121] [122] [123] [124]
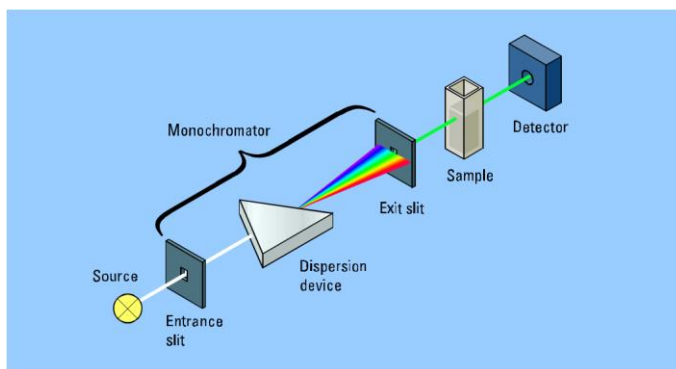
Figure 28. Scheme of UV-vis spectroscopy. [Source: Miramar College [130]]

In order to measure the photocatalyitic activity of the samples is necessary prepare the methyl orange (MO) with a concentration of 0,01 g/l and the powders of the different sols, as be explained in previous sections (2.5.1). Different bags are prepared with 0,05g of each sol and 5 ml of MO (Fig. 29). After that, the bags were put under light: ultraviolet (125-W UV lamp) and visible (45-W daylight lamp) to see the influence of each one causes in the samples.

Figure 29. Changing in the samples during photocatalytic activity measurements.

To know if MO was degraded over the time, the transmittance spectra were measured in the range of 350 to 500 nm or 600 nm by UV-vis spectrophotometer (Genesys 10S UV-vis) every hour for four hours. However, before of measure the transmittance is necessary centrifuge the samples to avoid the powders change the results guaranteeing that in the cuvette of the spectrophotometer there is only liquid.

2. RESULTS AND DISCUSSION

2.1. OPTICAL MICROSCOPY

The OM allows evaluating the quality of the coatings analysing the surface and the particles distribution. On the one hand, it has evaluated the picture of the three component sols (Fig. 30) establishing that the zinc had some undissolved particles and it presented with cracks in the surface; for this reason, the sol preparation procedure was changed, by adding a bit quantity of diethanolamine [95] and applying ultrasound to improve the quality of coatings.
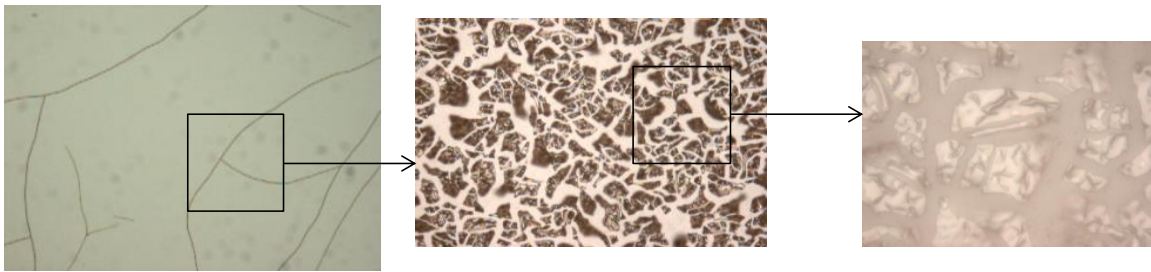
Figure 30. OM picture of $TiO_2 - SiO_2 - ZnO$ samples.

On the other hand, it has taken picture of four components slides ($TiO_2 - SiO_2 - ZnO - SnO_2$) without and with surfactants (Fig. 31). So as can be seen in one (a) and three (b) coatings pictures, ultrasound and diethanolamine helped zinc acetate to be dissolved completely because in the pictures do not appear conglomerates; however the samples still have cracks.

In addition, the four components slides those have added surfactants: Ethylactate, Poliethinlenglicol and Triton X-100 (Fig. 19 c, d, e, f, g, h, respectively) lack macrodefects such as cracks or voids and they have a high homogeneity in the distribution of the particles. And if the types of surfactants are compared, the three layers sample of Ethyllactate has some defect and the particle distribution is less compact and homogeneous. Also, the distribution of the particles in the other two surfactants improves considerably, being better in the Triton X-100 slide.
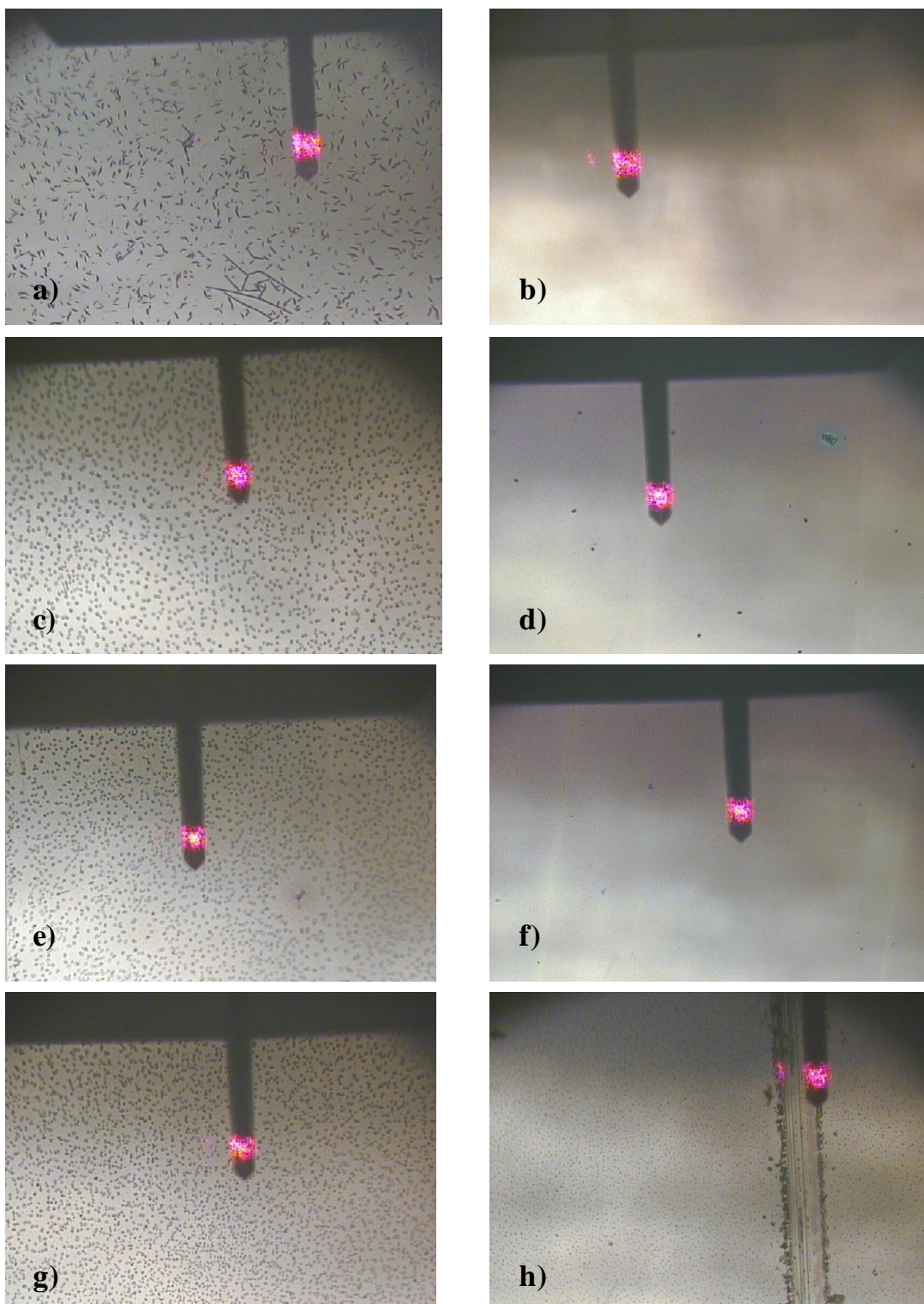
Figure 31. OM pictures of $TiO_2 - SiO_2 - ZnO - SnO_2$ samples. a) Without surfactant 1 layer. b) Without surfactants 3 layers. c) Ethyllactate 1 layer. d) Ethyllactate 3 layers. e) Polyethilenglicol 1 layer. f) Polyethilenglicol 3 layers. g) Triton X-100 1 layer. h) Triton X-100 3 layers.

2.2.X-RAY DIFRACTION

The crystal structure of all systems was analysed through X-ray diffraction in order to identify the phase and crystallinity of the samples. In addition, the crystal size (Table 5 and 6) was calculated using the *Scherer Equation* as is explained in 2.2.1.

2.2.1. Crystal size calculations

The Scherer equation is a formula that relates the size of particles or crystallites in a solid to the broadening of a peak in a diffraction pattern. The formula is:

$$\tau = \frac{K \cdot \lambda}{\beta \cdot \cos \theta}$$

Where:

- τ is the crystal size expressed in nanometers.
- K is a dimensionless shape factor. The typical value is 0,9.
- λ is the X-ray wavelength. The value is 1,54 nm.
- β is the line broadening at a half the maximum intensity, after subtracting the instrumental line broadening. The value is expressed in radians.
- θ is the Bragg angle (where is the peak).

Moreover, it is necessary to do the procedure that is shown in Figure 32 to obtain β (distance between discontinuous green lines in the graph expressed in radians).
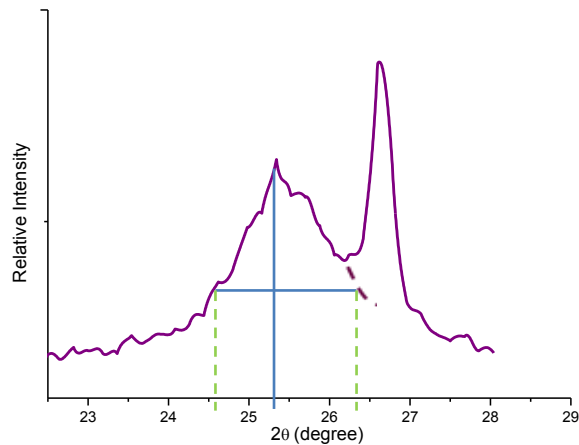
Figure 32. Example crystal size calculations.

Therefore, an example of calculation is:

$$\tau = \frac{K \cdot \lambda}{\beta \cdot \cos \theta} \ \rightarrow \ \tau = \frac{0,9 \cdot 1,54}{0,027 \cdot \cos 12,64} \ \rightarrow \ \tau = 51,09 \ nm$$

On the other hand the X-ray patterns (Figure 32 and 33) and the crystal size (Table 5 and 6) are shown below:
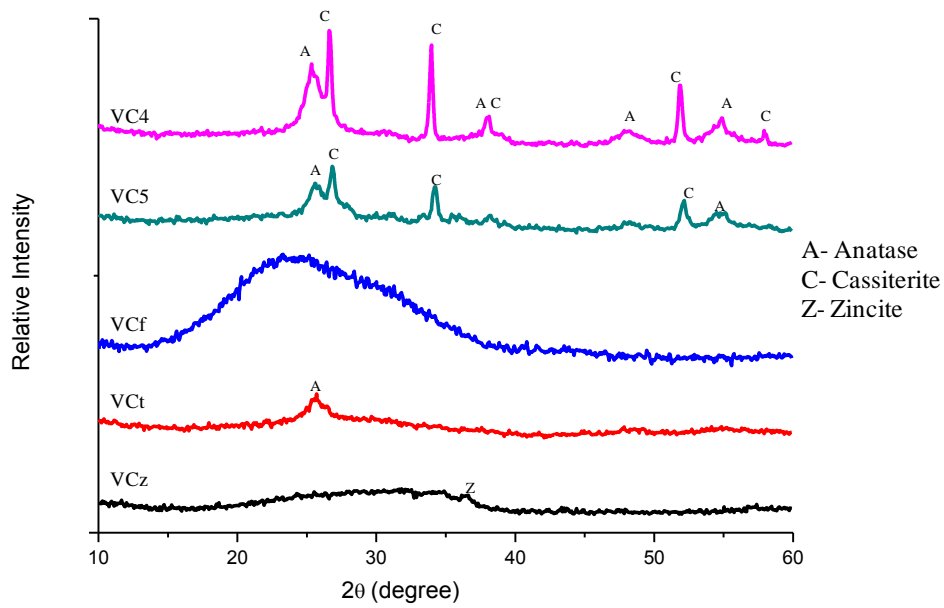
Figure 33. X-ray diffraction pattern of samples.

Table 5. Crystal size calculated by Sherer formula

Coatings	Crystalline phase	Crystal size (nm)
VC$_z$	Zincite	66,07
VC$_t$	Anatase	41,68
VC$_5$	Anatase	60,92
	Cassiterite	117,43
VC$_4$	Anatase	51,09
	Cassiterite	146,79
VC$_f$	amorphous	-

The X-ray measurement revealed that the three components sample VC_f presents an amorphous structure; and although the peak in VC_t is not very narrow, it means that this sample has nanosized TiO_2 phase (41,68 nm), with low crystallinity. VC_z has the very small elevation in place corresponds to the 100% ZnO main maximum (36,25º), but the crystallinity is very low or the size of the crystals is too small (66,07 nm).

The diffraction pattern of the other samples indicates, as the same way that VC_t, the presence of anatase at the highest peak in $2\Theta = 25,28º$, being more intensive in VC_4 samples with a crystal size of 51,09 nm. Also, they show another anatase peaks (37,8º,48,05º and 55,06º). In relation with SnO_2 crystallinity different peaks of cassiterite (26,61º, 33,89º and 51,78º) can be seen in four and five components samples throughout the X-ray pattern, with a bigger crystal size than anatase (117,43 and 146,79 nm)
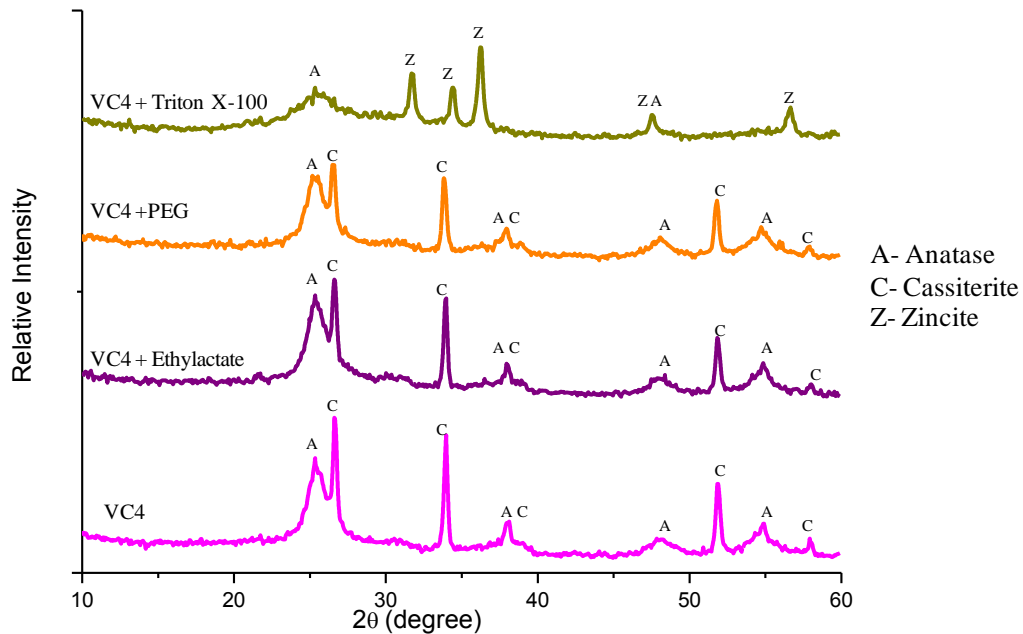
Figure 34. X-ray diffraction pattern of VC_4 and VC_4 with surfactants.

Table 6. Crystal size of VC_4 and VC_4 with surfactants.

Coatings	Crystalline phase	Crystal size (nm)
VC_4	Anatase	51,09
	Cassiterite	146,79
VC_4 + Ethylactate	Anatase	49,50
	Cassiterite	130,48
VC_4 + PEG	Anatase	56,57
	Cassiterite	158,69
VC_4 + Triton X-100	Anatase	36,84
	Zincite	148,66

On the other hand, comparing the VC_4 results with and without surfactants can be established that the VC_4 without surfactants present the more intensive peaks. VC_4 and VC_4 with three types of surfactants Ethyllactate, polyethyleneglicol and Triton X-100 are very similar, however it seems that Triton X-100 encourage zincite phase crystallization and less anatase and cassiterite. The crystal size in all of them is very similar, being a little bigger in VC_4 with PEG.

2.3. ATOMIC FORCE MICROSCOPY (AFM)

The films morphology and surface structure were investigated by AFM. Three and four components system are compared below. Also roughness, bearing ratio, surface area and thickness was calculated (Appendix 1) using Image Processing v 2.1 software. The average results are presented in Table 7.

Figure 35. AFM images of VC$_z$ coatings in 2D and 3D mode: a) 60 mm/min-1 layer, b) 60 mm/min-3 layers, c) 220 mm/min-1 layer, d) 220 mm/min-3 layers.

VC$_z$ coatings were transparent and homogeneous. Figure 35 shows the surface morphology of VC$_z$ coatings. The morphology of thin films at slow coating rate forming sharp particles on the surface with the same particle size ($\sim$500 nm) in both cases (1 and 3 layers) and a homogenous distribution with more or less the same surface area; however the roughness is bigger in 3-layers. As the same way, the 1 layer at fast rate has sharp particles too, however 3 layers present cracks in the surface increasing considerably the roughness. Also, the thickness of slides was calculated, and they are thin.
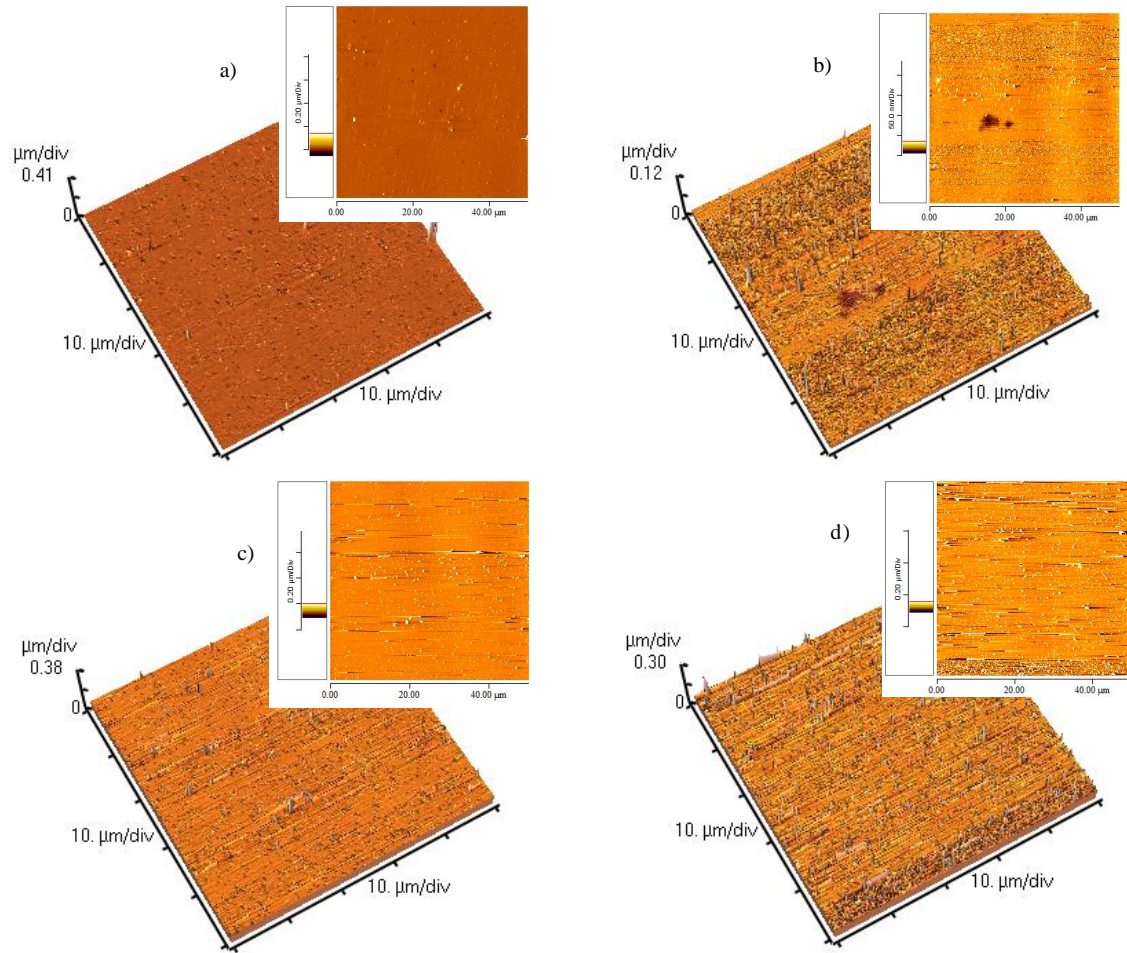
Figure 36. AFM images of VC$_t$ coatings in 2D and 3D mode: a) 60 mm/min-1 layer, b) 60 mm/min-3 layers, c) 220 mm/min-1 layer, d) 220 mm/min-3 layers.

The appearance of the slides was transparent and homogeneous. As can be seen in Figure 36, the morphology of VC$_z$ coatings is homogeneous in all cases, without any imperfection. Regarding to the roughness and bearing ratio are bigger at fast rate, exceeding the 80% of data points 158, 98 and 132,76 nm of height.
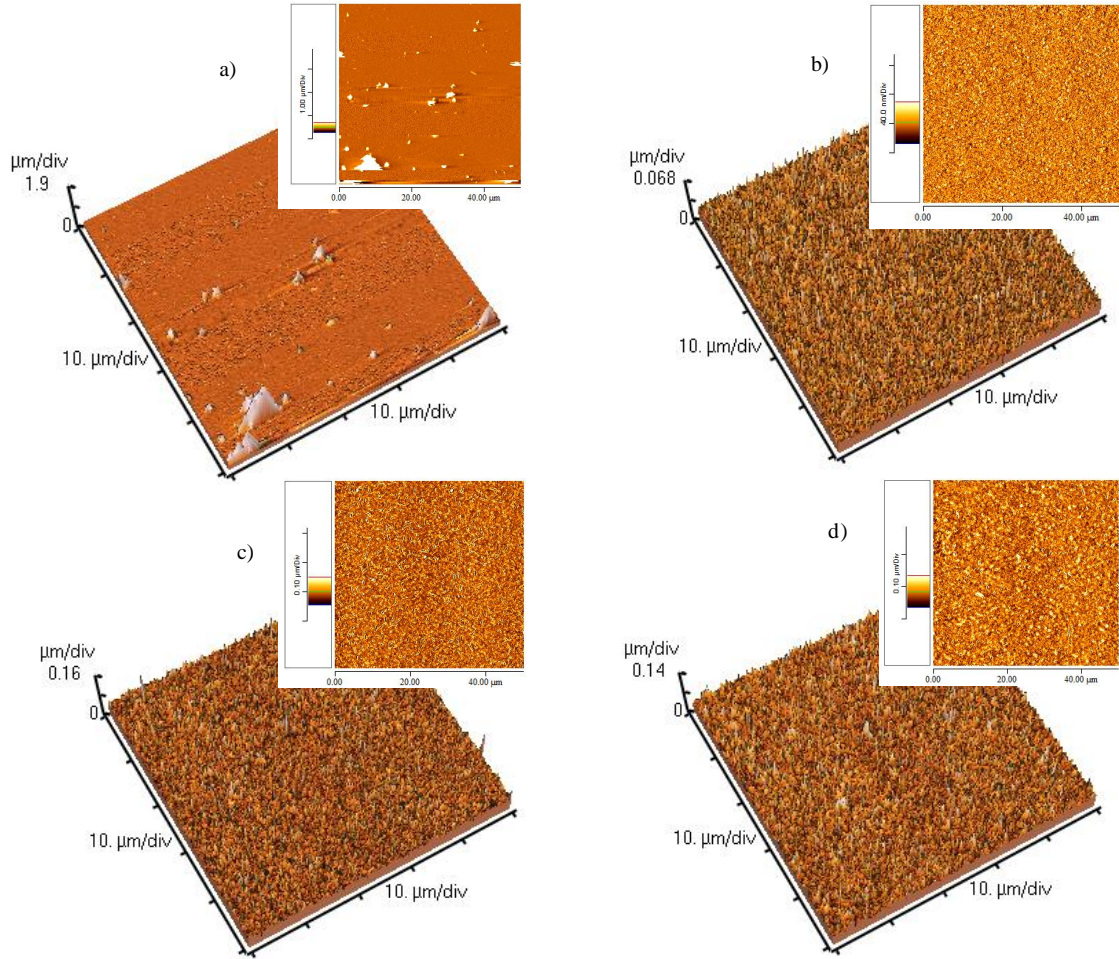
Figure 37. AFM images of VC_f coatings in 2D and 3D mode: a) 60 mm/min-1 layer, b) 60 mm/min-3 layers, c) 220 mm/min-1 layer, d) 220 mm/min-3 layers.

Regarding to VC_f coatings they were transparent orange, increasing the tone at fast rate and 3 layers. The $VC_{f\ morphology}$ can be seen in Figure 37, the fast rate coatings have cracks on the surface and because of that, the roughness is much bigger than at slow rate. Nevertheless, the slow rate coatings have not any imperfection, although the particles are not clearly visible and the bearing ratio of the first sample is remarkably big.
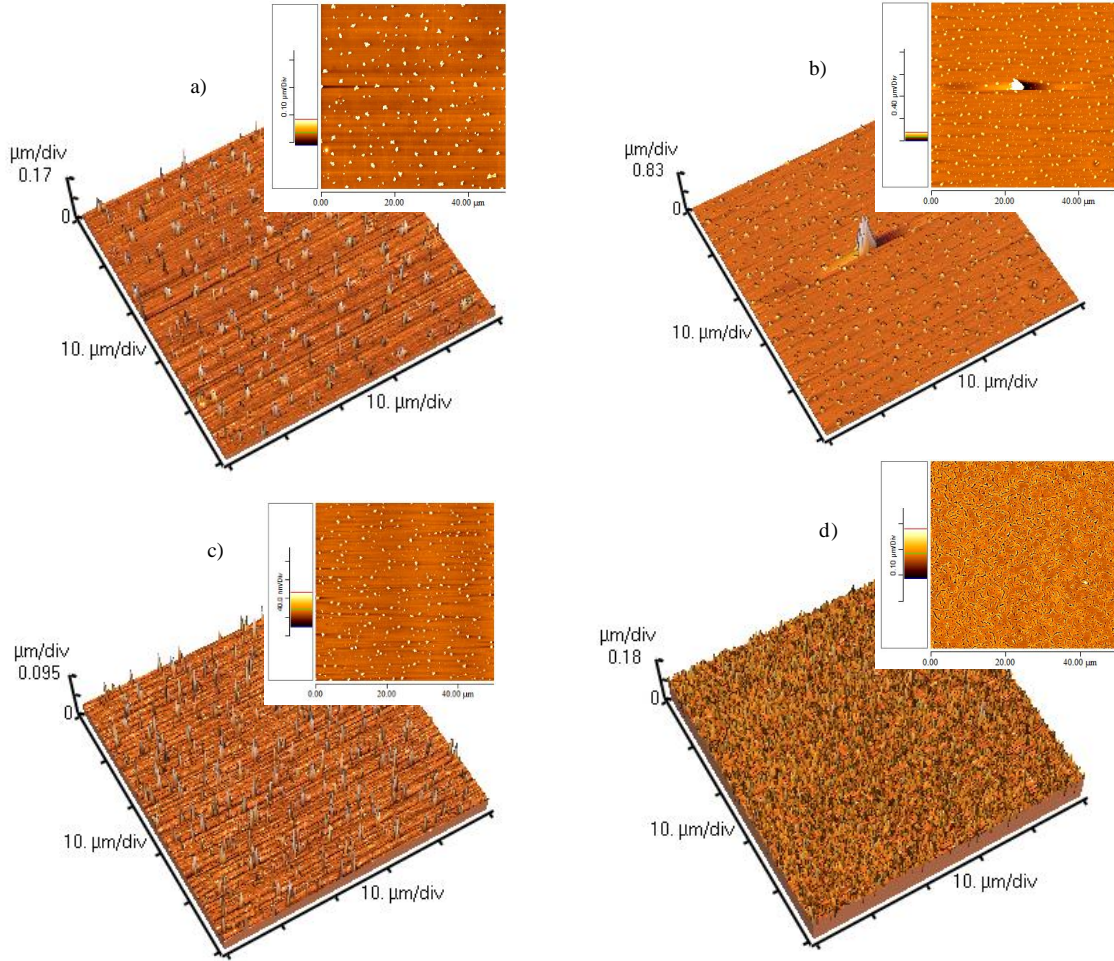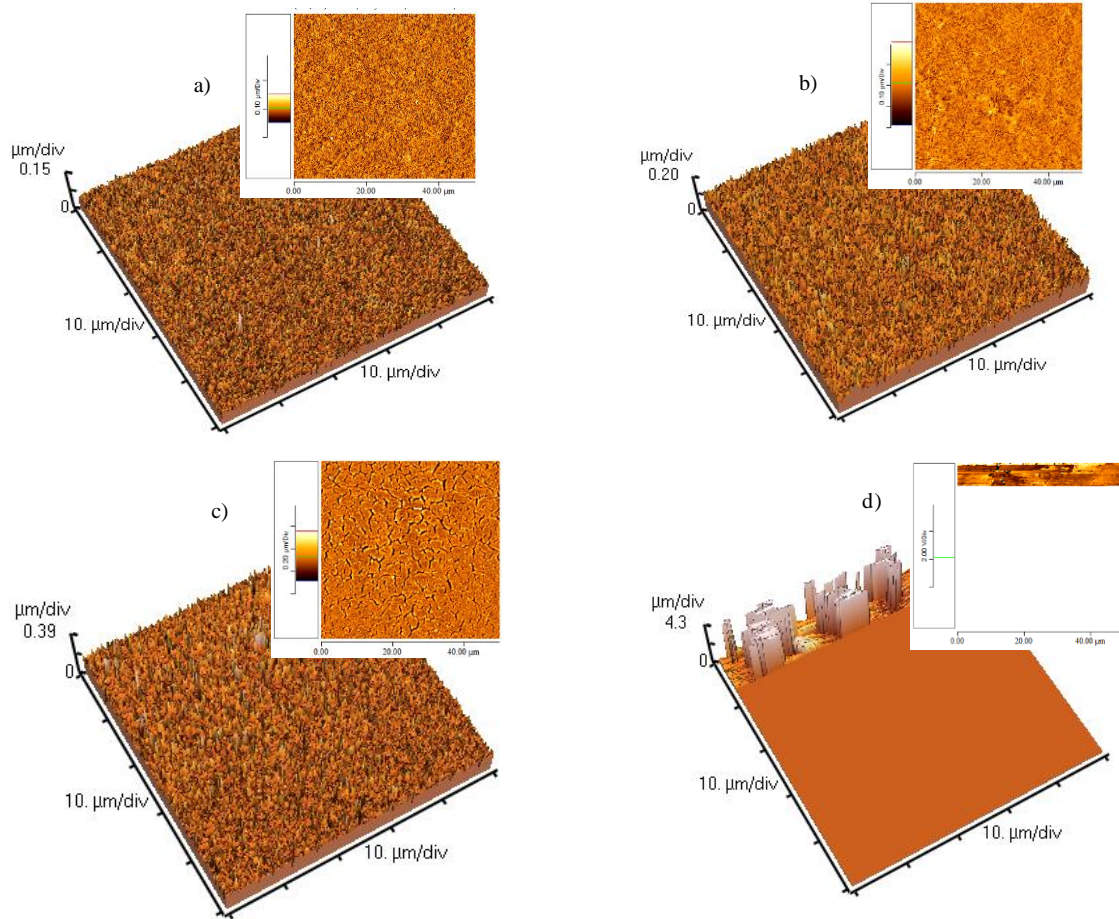
Figure 38. AFM images of VC$_5$ coating in 2D and 3D mode: a) 60 mm/min-1 layer, b) 60 mm/min-3 layers, c) 220 mm/min-1 layer, d) 220 mm/min-3 layers.

The appearance was transparent in 1 layer, and a little transparent brown in 3 layers at both rates. The morphology (Figure 38) of the slow rate coatings homogeneous, but the particles are formed very closely and densely, for this reason the roughness of VC$_5$ is bigger than the others coatings. However, the coatings at fast rate present cracks over the surface and the roughness is bigger than slow coatings rate, as can be seen in Table 7.

Table 7. Characteristics of the surface from AFM image at 50x50

Sample	Roughness (nm)	Bearing ratio 30% (nm)	Bearing ratio (80%) (nm)	Surface area (μm^2)	Thickness (nm)
VC_Z 60x1	4,42	32,08	29,77	2507	25,42
VC_Z 60x3	6,09	95,24	91,51	2517	87,82
VC_Z 220x1	3,71	53,03	50,22	2506	49,51
VC_Z 220x3	20,35	193,15	169,35	2625	169,78
VC_T 60x1	1,66	34,78	33,06	2504	114,5
VC_T 60x3	2,22	26,13	23,4	2504	216,75
VC_T 220x1	3,7	162,18	158,98	2512	119,43
VC_T 220x3	5,69	138,79	132,76	2524	242,33
VC_F 60x1	4,81	507,1	498,58	2636	105,52
VC_F 60x3	7,37	47,52	35,75	2510	225,26
VC_F 220x1	12,84	105,76	88,71	2530	106,3
VC_F 220x3	12,86	84,68	73,69	2523	247,4
VC_5 60x1	14,09	109,87	87,05	2536	98,98
VC_5 60x3	32,11	225,56	171,15	2640	142,11
VC_5 220x1	48,67	348,92	281,29	2743	297,6
VC_5 220x3	*The images were corrupted*				

Regarding to the results that appear in Table 7, the roughness of all samples is bigger at fast rates and usually bigger with 3 layers, nevertheless, the roughness changes when come cracks appear in the surface, increasing considerably the value. Nevertheless, the bearing ratio does not depend on the rates and layers; it only depends of the height.

On the other hand, the surface area is between 2500 and 2750 nm. And the thickness changes from one sample to another, but always are thicker at slow rate and 1 layer.
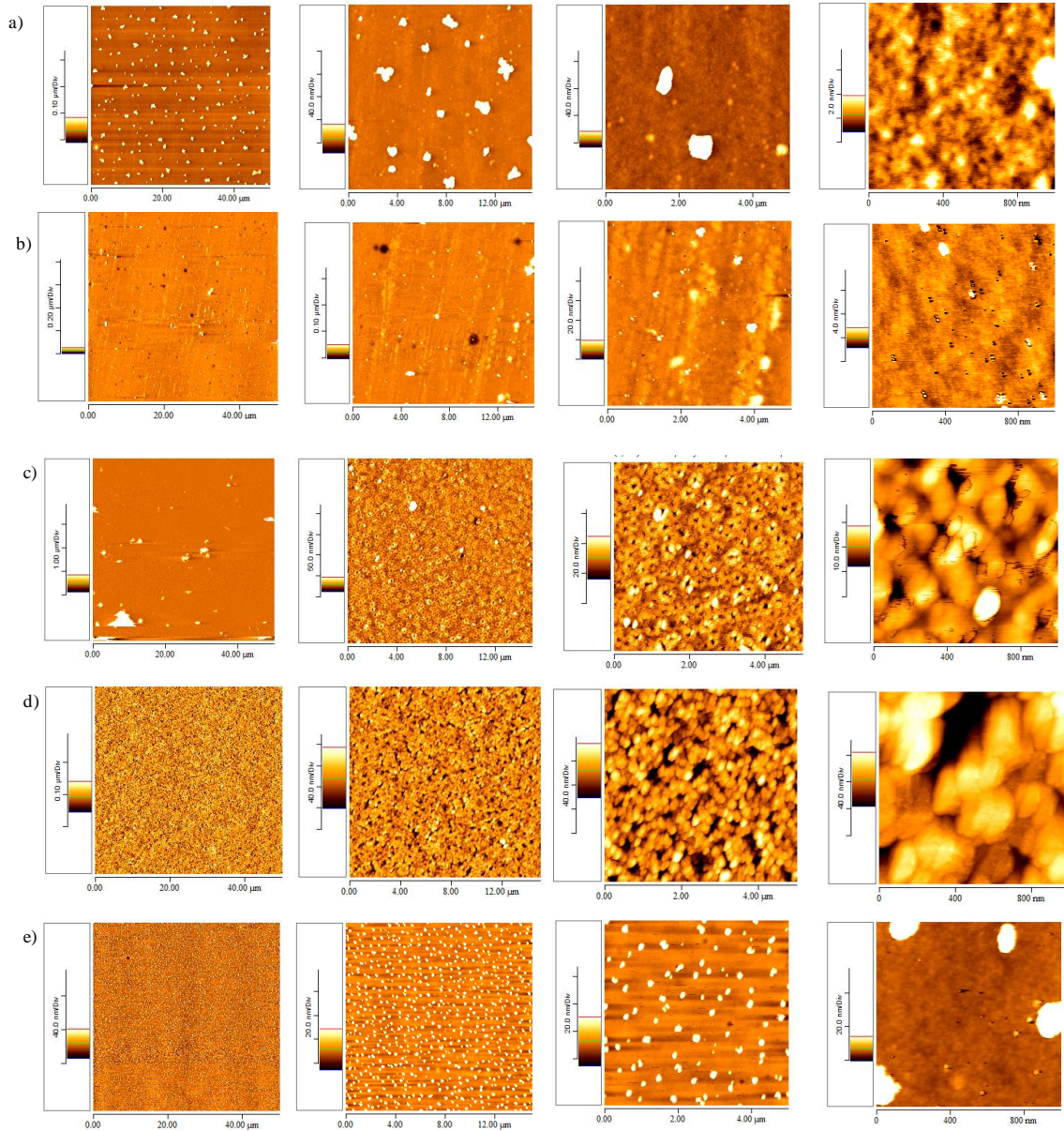
Figure 39. Best coatings in AFM with a scanning area of 50x50, 15x15, 5x5 and 1x1 μm in 2D, from the left to right, respectively: a) VC_z at 60 mm/min-1 layer, b) VC_t at 60 mm/min-1 layer, c) VC_f at 60 mm/min-1 layer, d) VC_5 at 60 mm/min-1 layer.

In Figure 39 appear images of the best coating of each sol: VC_z at 60 mm/min-1 layer, VC_t at 60 mm/min-1 layer, VC_f at 60 mm/min-1 layer and VC_5 at 60 mm/min-1 layer; in which it can be seen the morphology of the coatings with more details. Therefore, the particle size of the coatings is presented in the right images, being bigger in VC_5 and

smaller in VC_t; and the distribution of the particles that can be explained by the particle nucleation mechanism after the drying of each coating layer.
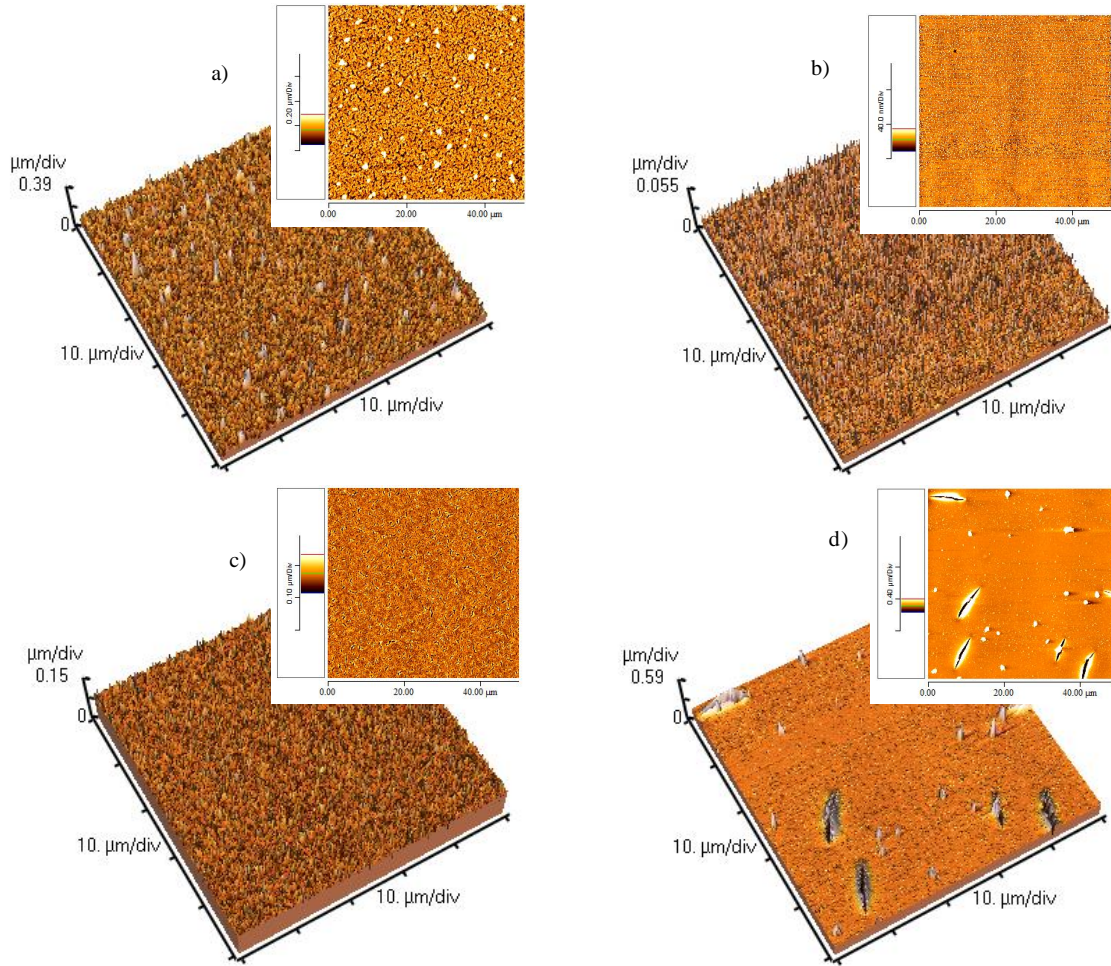
Figure 40. AFM images of VC_4 coatings in 2D and 3D mode: a) 60 mm/min-1 layer, b) 60 mm/min-3 layers, c) 220 mm/min-1 layer, d) 220 mm/min-3 layers.

The appearances of the slides were transparent in 1 layer coatings, semitransparent in 60 mm/min-3 layers and completely dark brown in the other one. The morphology of VC_4 can be seen in Figure 40, the 1 layer coatings have cracks over the surface, which explains them high roughness (39,5 and 13,55 nm) respectively compared with 3 layers. On the other hand, the surfaces of 3 layers coatings only have some isolated cracks, could be appeared them because of the constrained shrinkage of a thin ceramic coating during sintering, that it reflected in intergranular friction influences the rearrangement behaviour of particles and hence indirectly affects the formation of cracks.
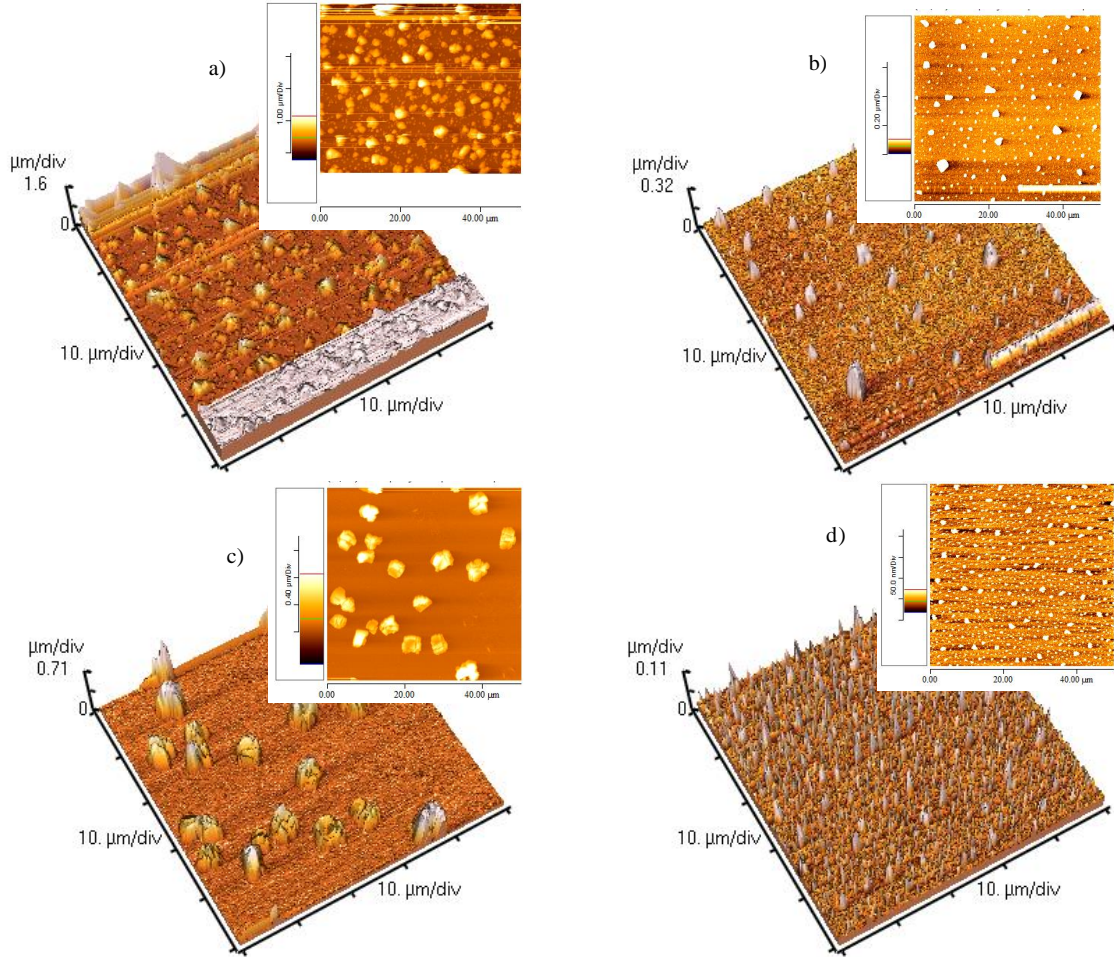
Figure 41. AFM images of VC$_4$ with Ethylactate coatings in 2D and 3D mode: a) 60 mm/min-1 layer, b) 60 mm/min-3 layers, c) 220 mm/min-1 layer, d) 220 mm/min-3 layers.

The morphology of VC$_4$ with Ethylactate coating is shown in Figure 41. The 3 layers coatings have sharper and smaller particles (~1500μm) than the 1 layer coatings (~2500μm), for that the roughness is much bigger (Figure 43). In addition, any coating present cracks unlike VC$_4$ without surfactants, because surfactants reduce the interaction of forces between the liquid and the particles, avoiding that appear cracks during the drying or sintering.
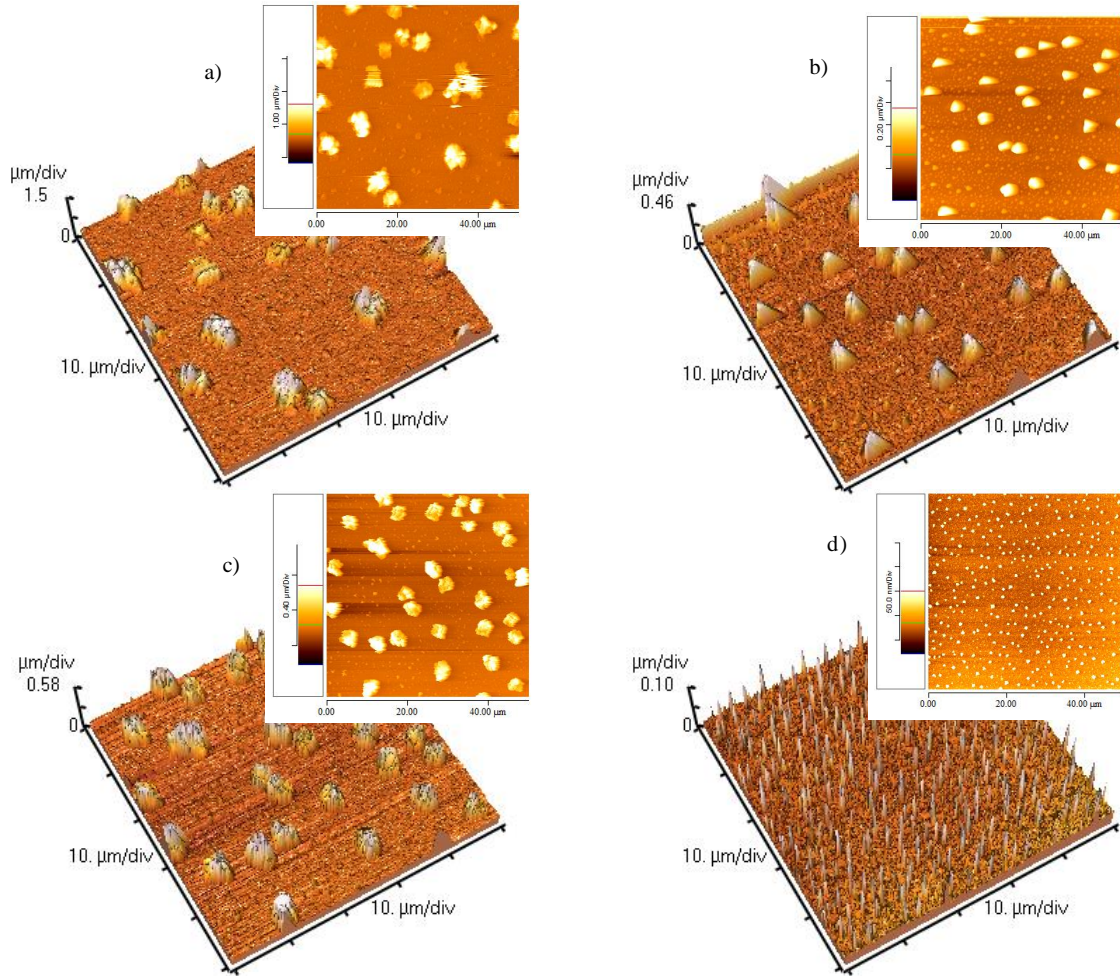
Figure 42. AFM images of VC$_4$ with PEG in 2D and 3D. a) 60 mm/min-1 layer, b) 60 mm/min-3 layer, c) 220 mm/min-1 layer, d) 220 mm/min-3 layer.

As the same way that Ethyllactate, PEG (Figure 42) helps to avoid the cracks on the surface and the coatings present approximately the same appearance: sharp particles in 3 layers and round in 1 layer. Also, the roughness is bigger in 1 layer.
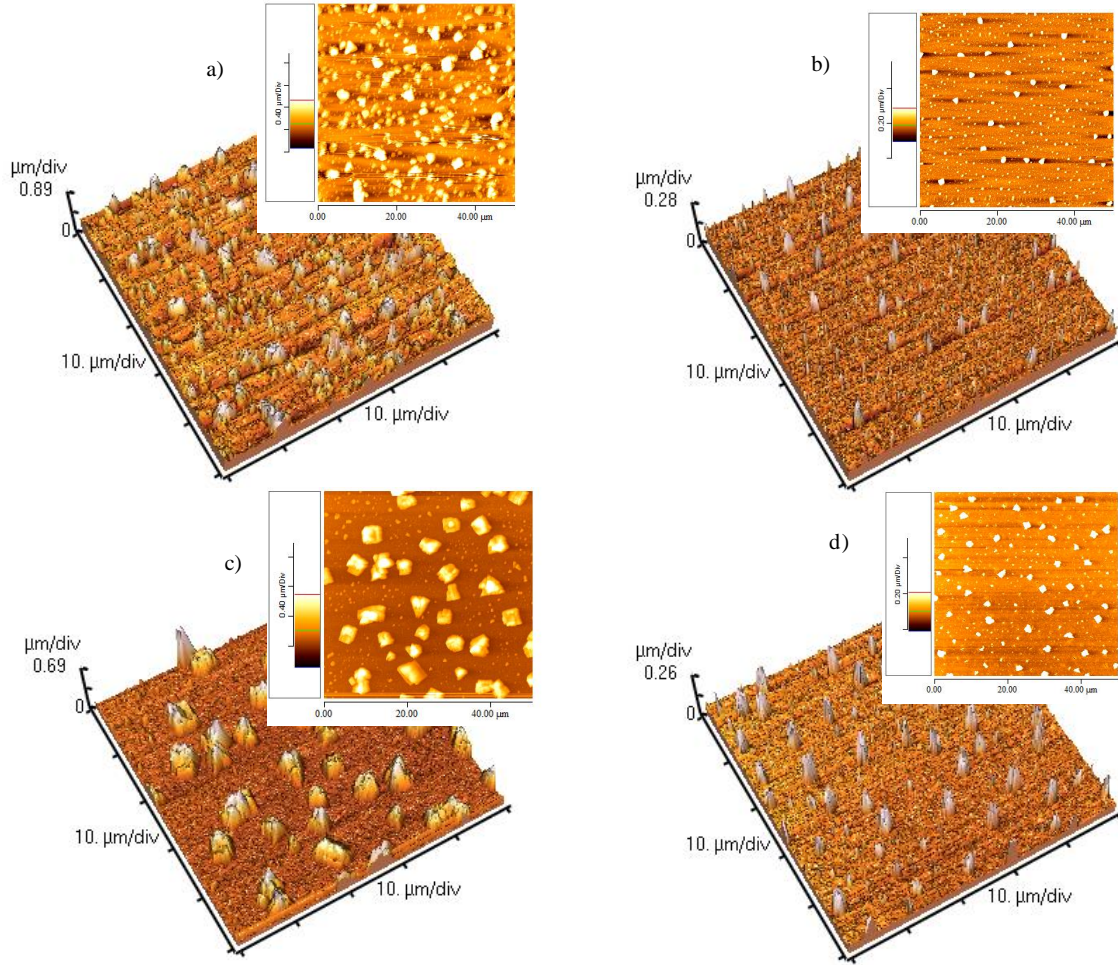
Figure 43. AFM images of VC$_4$ with Triton X-100 in 2D and 3D. a) 60 mm/min-1 layer, b) 60 mm/min-3 layer, c) 220 mm/min-1 layer, d) 220 mm/min-3 layer.

VC$_4$ with Triton X-100 morphology is shown above. The images shown that the particles are evenly distributed in the surface of all samples, however the slow rate- 1 layer has much more quantity of particles. In addition, the difference between sample roughness is similar than the other two surfactants.
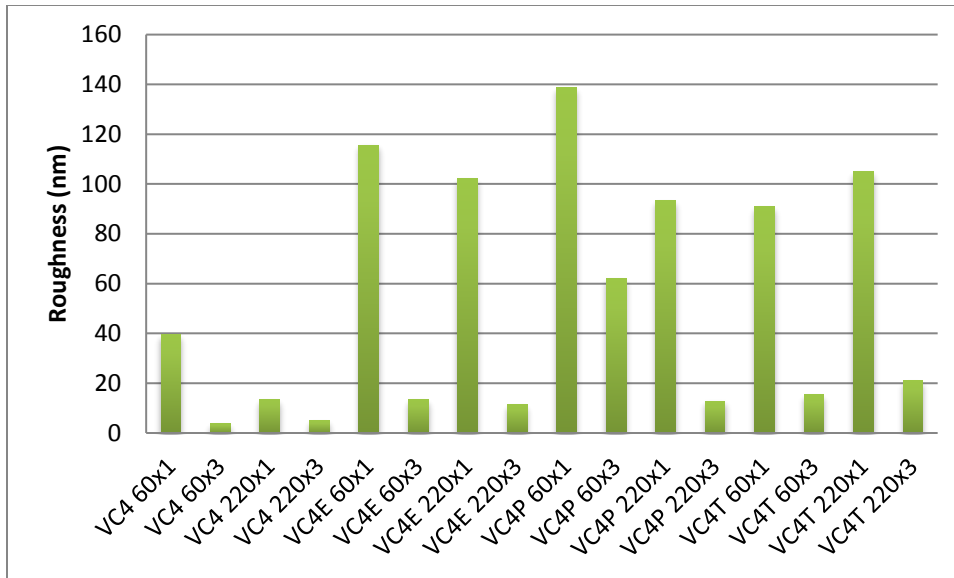
Figure 44. Roughness of VC₄ coatings with and without surfactants.

The roughness, surface area and thickness of VC₄ samples appear in Figures 44, 45 and 46. Regarding to the roughness is bigger at 1 layer in all samples and it increases considerably with the surfactants were added; also it exits differences between surfactants, being PEG that causes the biggest.
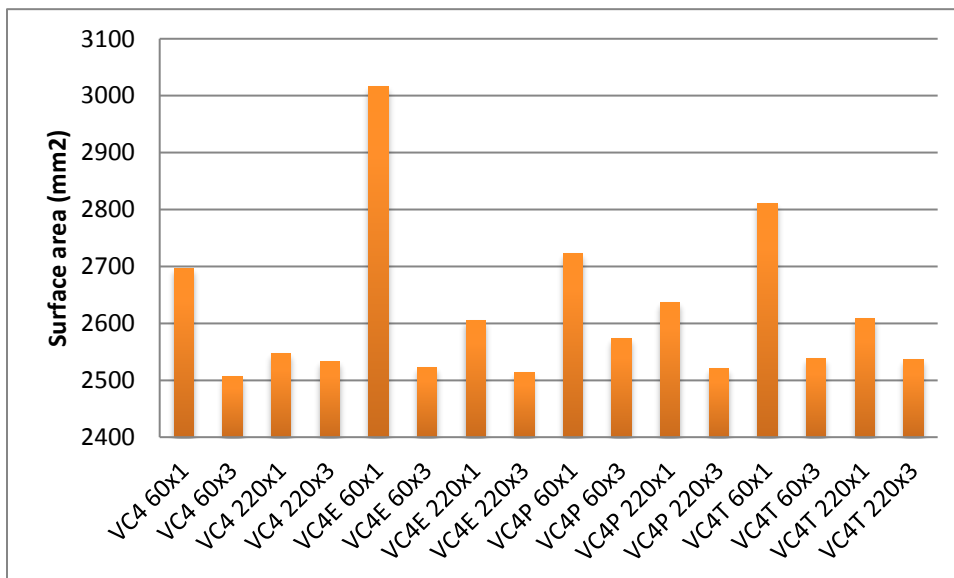
Figure 45. Surface area of VC₄ coatings with and without surfactants.
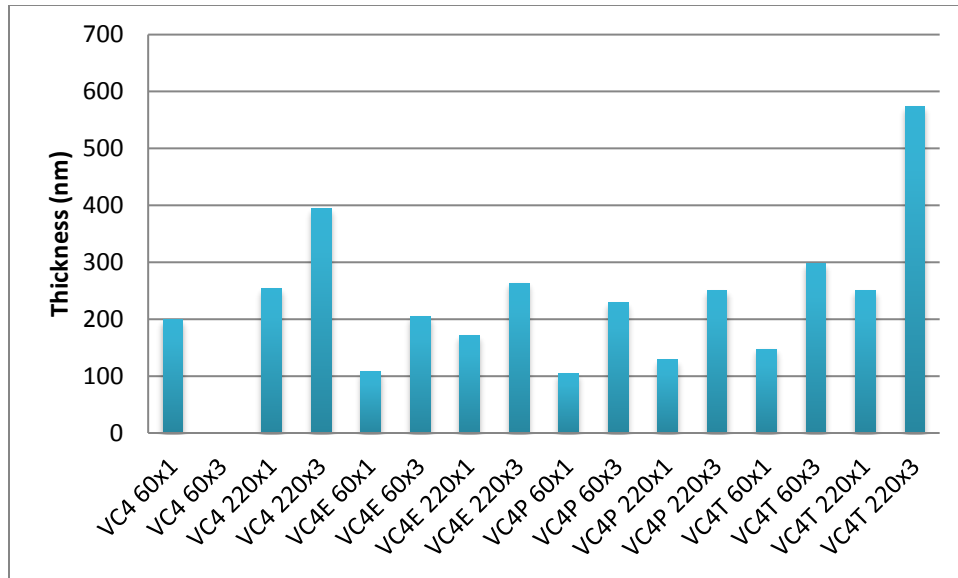
Figure 46. Thickness of VC$_4$ coatings with and without surfactants.

The surface area does not depend on the rates and layers and it present approximately the same value in all samples. And the thickness was the result that it expected, is always thicker at slow rate and 1 layer; and the same way that roughness, the thickness is bigger in VC$_4$ with surfactants.

In Figure 47 appear morphology's images of the best coatings of VC$_4$ with more details, being slow rate and 3 layers the best of VC$_4$ without surfactants and fast rate and 1 layer for the samples that contain surfactants. In relation with the distribution of the particles is homogeneous in all samples, being the small particles bigger in the samples containing surfactants and being the PEG that cause the smallest particles and more porous coatings. In addition, any coating presents cracks and any other imperfection.
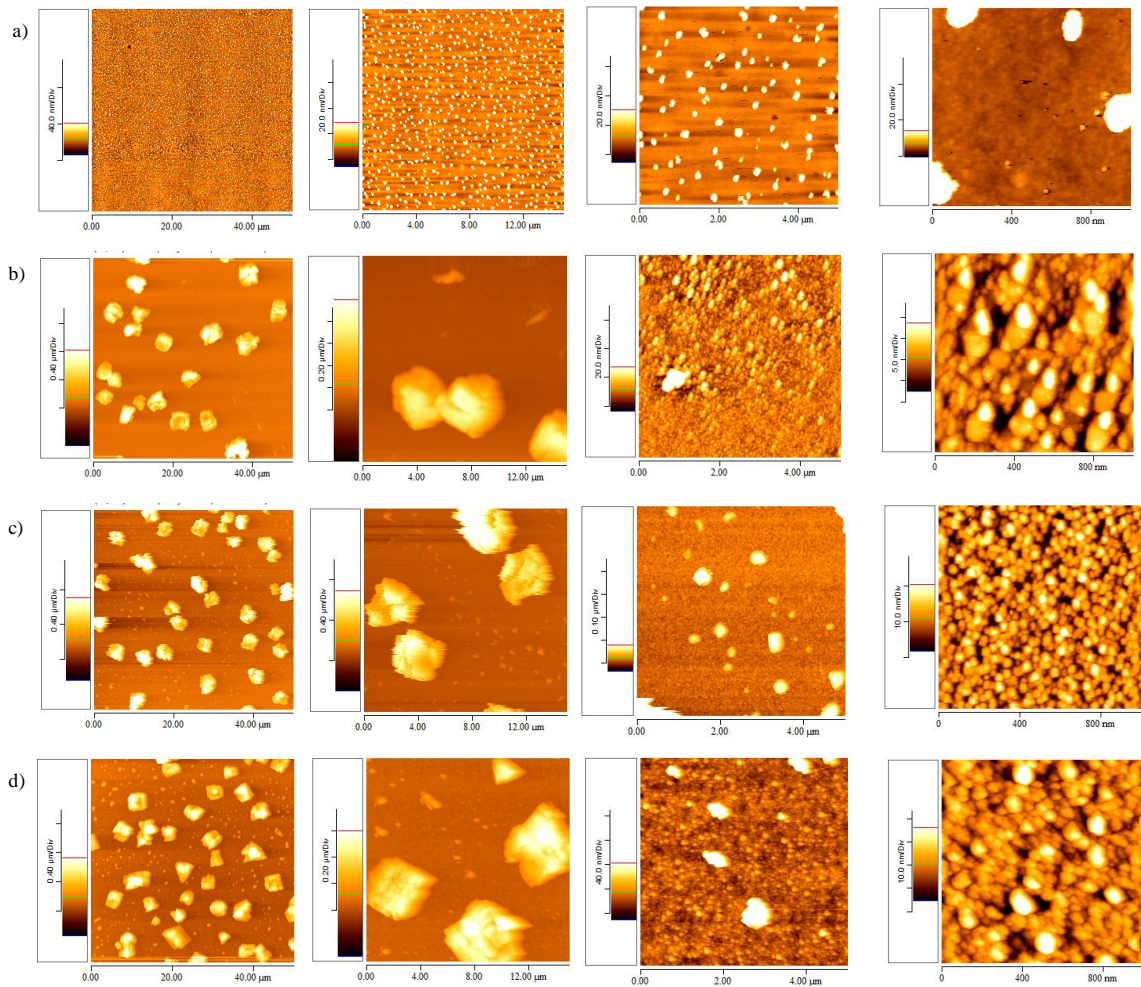
Figure 47. Best coatings in AFM 50x50, 15x15, 5x5 and 1x1 in 2D: a) VC_4 at 60 mm/min-3 layer, b) VC_4 with Ethyllactate at 220 mm/min-1 layer, c) VC_4 with PEG at 220 mm/min-1 layer, d) VC_4 with Triton X-100 at 220 mm/min-1 layer.

2.4. SCANNING ELECTRON MICROSCOPY (SEM)

The morphology of nanofilms was characterized by SEM.

SEM images of three components coatings are shown in Figures 48 and 49. According to Figure 48 it can be seen that three component slides with tin lack of cracks and present spherical crystalline particles, however Figure 48 shows that zinc slides present cracks. Comparing homogeneity of both samples, the VC_t coating tin has more homogeneity.

On the other hand, comparing particle size obtained with AFM and SEM (Table 8) it can be establishing that the AFM results are measured with more accuracy. Moreover, comparing the results, the particle size with 3 layers and fast rate is smaller in all cases.
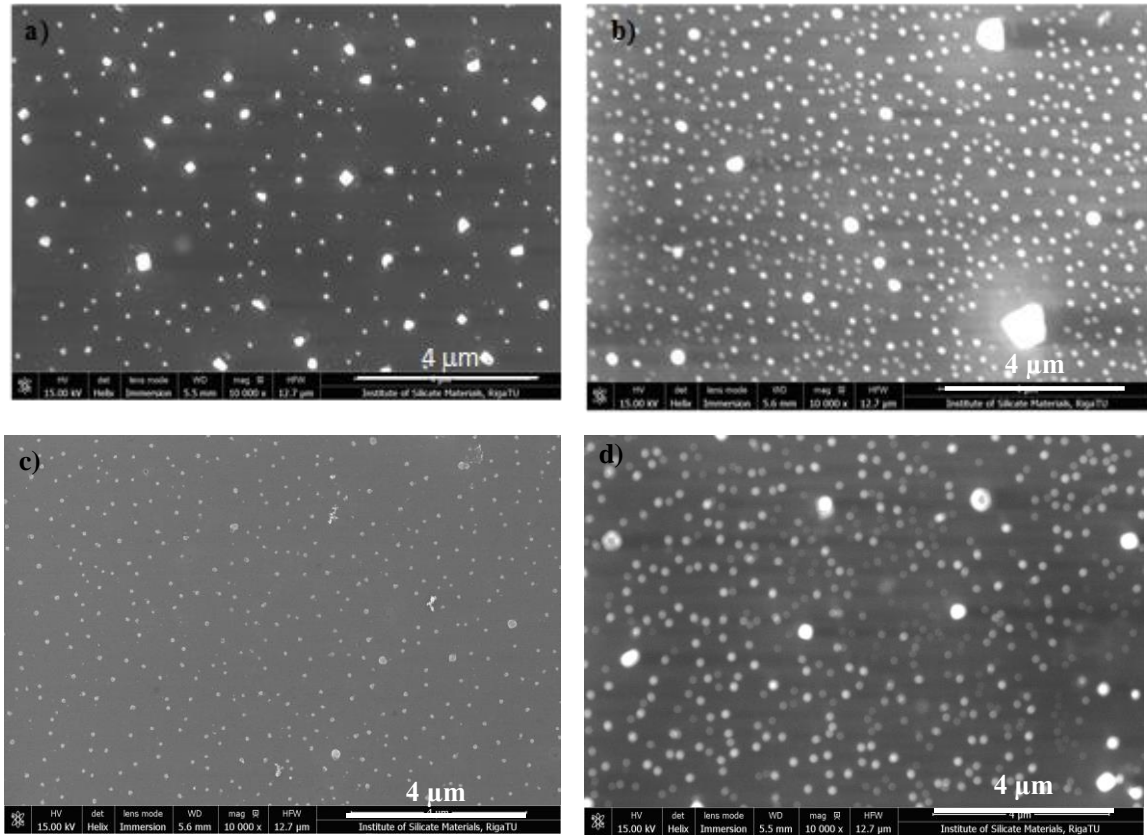
Figure 48. SEM images of VC$_t$ coatings: a) 60 mm/min 1 layer, b) 60 mm/min 3 layers, c) 220 mm/min 1 layer, d) 220 mm/min 3 layers.
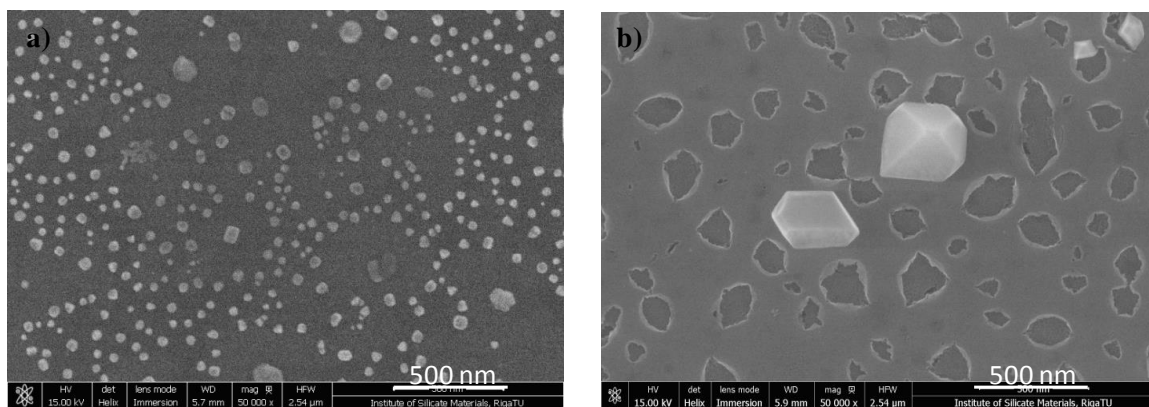
Figure 49. SEM images of VCz coatings: a) 220 mm/min 1 layer, b) 60 mm/min 1 layer.

Table 8: Particle sizes of VC_t and VC_z

Method of analysis	Dip-coating rate (mm/min)	VC_t Particle size (nm)	VC_z Particle size (nm)
AFM	60 x1	120- 350	150- 500
	60 x3	60- 250	-
	220 x1	50- 200	90- 550
	220 x3	20- 200	-
SEM	60 x1	100- 500	100- 350
	60 x3	100- 250	-
	220 x1	70- 320	50- 100
	220 x3	50- 120	-

In addition, four components SEM images are presented below. As can be observed in Figure 50 the coatings at fast rate, as one layer nanofilms present a lot of cracks over the surface (a and d). On the other hand, the surface of the three layers nanofilms have some big defects, only some isolated cracks, maybe because they have some big particle in one of the layers and during sintering the surface cannot support the stress; also the particles are considerably and homogeneously distributed all over the surfactants low dip-coating rate.

In addition, as the same way that VC_t and VC_z the particle size is presented in Table 9. The SEM results of 1 layer cannot be measured very well (*) because of the cracks but, also with results can be establish that the particle size with 3 layers and fast rate is smaller.
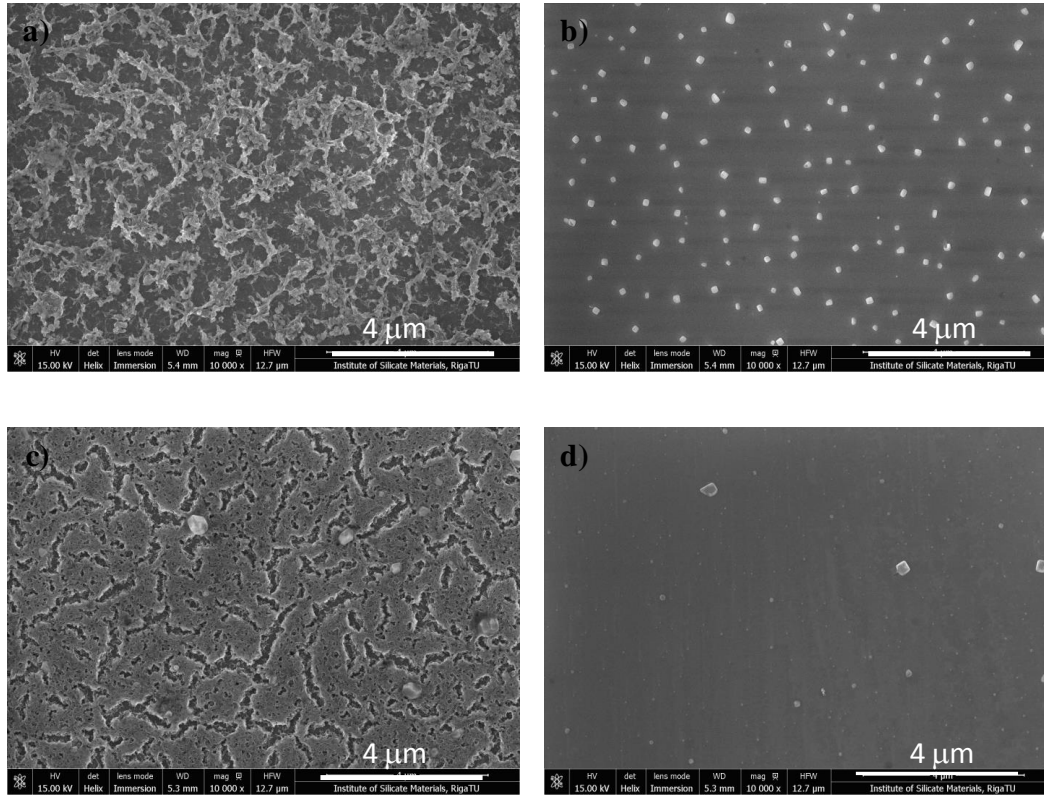
Figure 50. SEM images of VC$_4$ coatings. a) 60 mm/min 1 layer. b) 60 mm/min 3 layers. c) 220 mm/min 1 layer. d) 220 mm/min 3 layers.

Table 9. Particle sizes of VC$_4$.

Method of analysis	Dip-coating rate (mm/min)	VC$_4$ Particle size (nm)
AFM	60 x1	175- 300
	60 x3	50- 200
	220 x1	120- 140
	220 x3	100- 300
SEM	60 x1	75- 160 (*)
	60 x3	120- 250
	220 x1	275- 460 (*)
	220 x3	60- 300
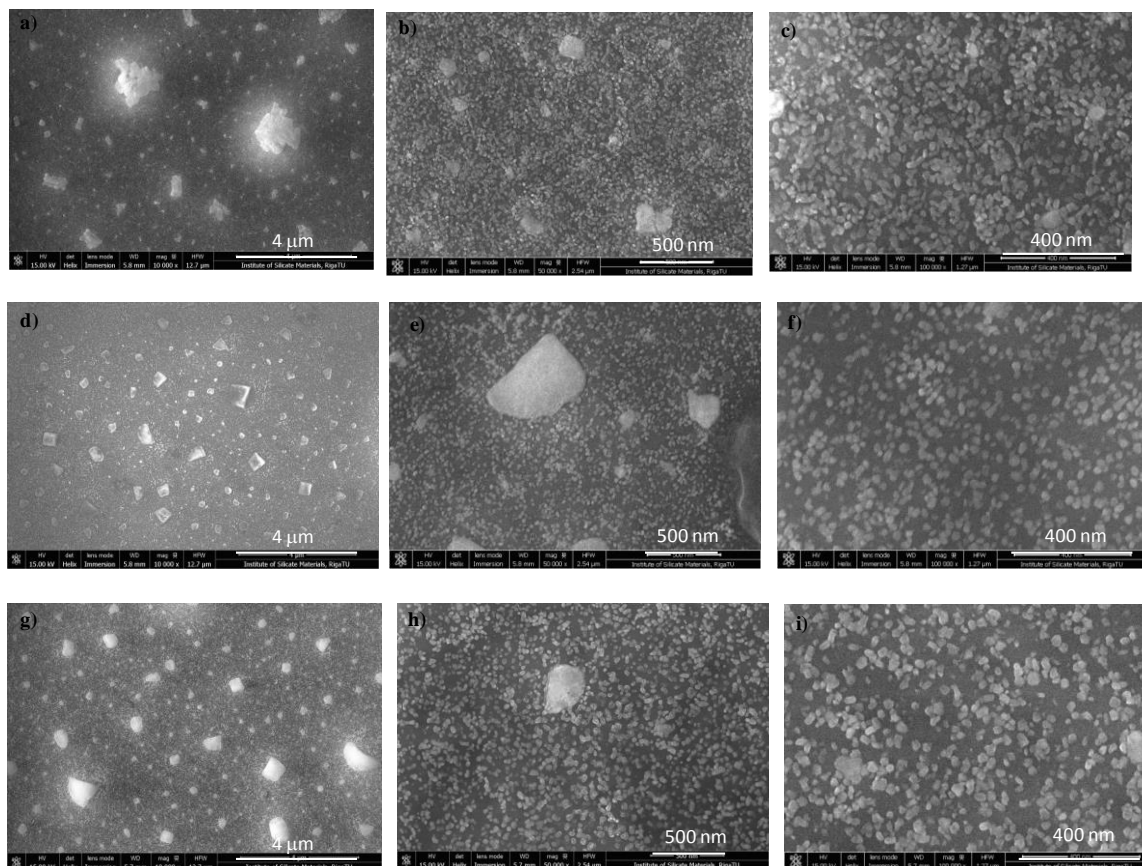
Figure 51. SEM images of VC$_4$ coatings with surfactants: a), b) and c) Ethyllactate, d), e) and f) PEG, g), h) and i) Triton X-100.

Table 10. Particle sizes of VC$_4$ with surfactants.

Method of analysis	Dip-coating rate (mm/min) 3x	Ethylactate (nm)	PEG (nm)	Triton X-100 (nm)
AFM	220	20- 500	40- 800	20- 500
SEM	220	20- 600	30- 950	40- 1000

In the case of four components with surfactants nanofilms, Figure 51, it is observed that the surface of nanofilm contains crystalline particles uniformly dispersed and the surface has not any cracks unlike four components without surfactant. Therefore, surfactants can be the solution to prevent the formation of cracks, because they reduce the interaction of forces between the liquid and the particles, avoiding that appear cracks during the drying or sintering.

Finally, if the three surfactants in the VC4 sol composition are compared, the ethyllactate has more nanosized and compact particle distribution than the others and it presents different size of particles (Table 10).

2.5.PHOTOCATALYTIC PROPERTIES

To know if the materials have photocatalytic properties, the transmittance (%) of the samples in MO is measured with a UV-vis spectrophotometer every hour.

Firstly, the results of degradation with ultraviolet light are presented (Fig. 52). The three components samples with zinc and iron (A, B) did not degrade the MO a lot under ultraviolet light over the time (every hour – 0, 1, 2, 3 and 4 h) this phenomenon seems to be due to the absence of crystalline phase as can be seen in the X-ray patterns. However, the three components with tin oxide sample (C) degraded the MO because of the presence of anatase and with the increases the irradiation time the concentration of MO gradually decreases.

In addition, four and five components samples (D, E) present a very good photocatalytic activity; the MO was completely degraded in the first hour in four component cases and in the second hour in the five components.
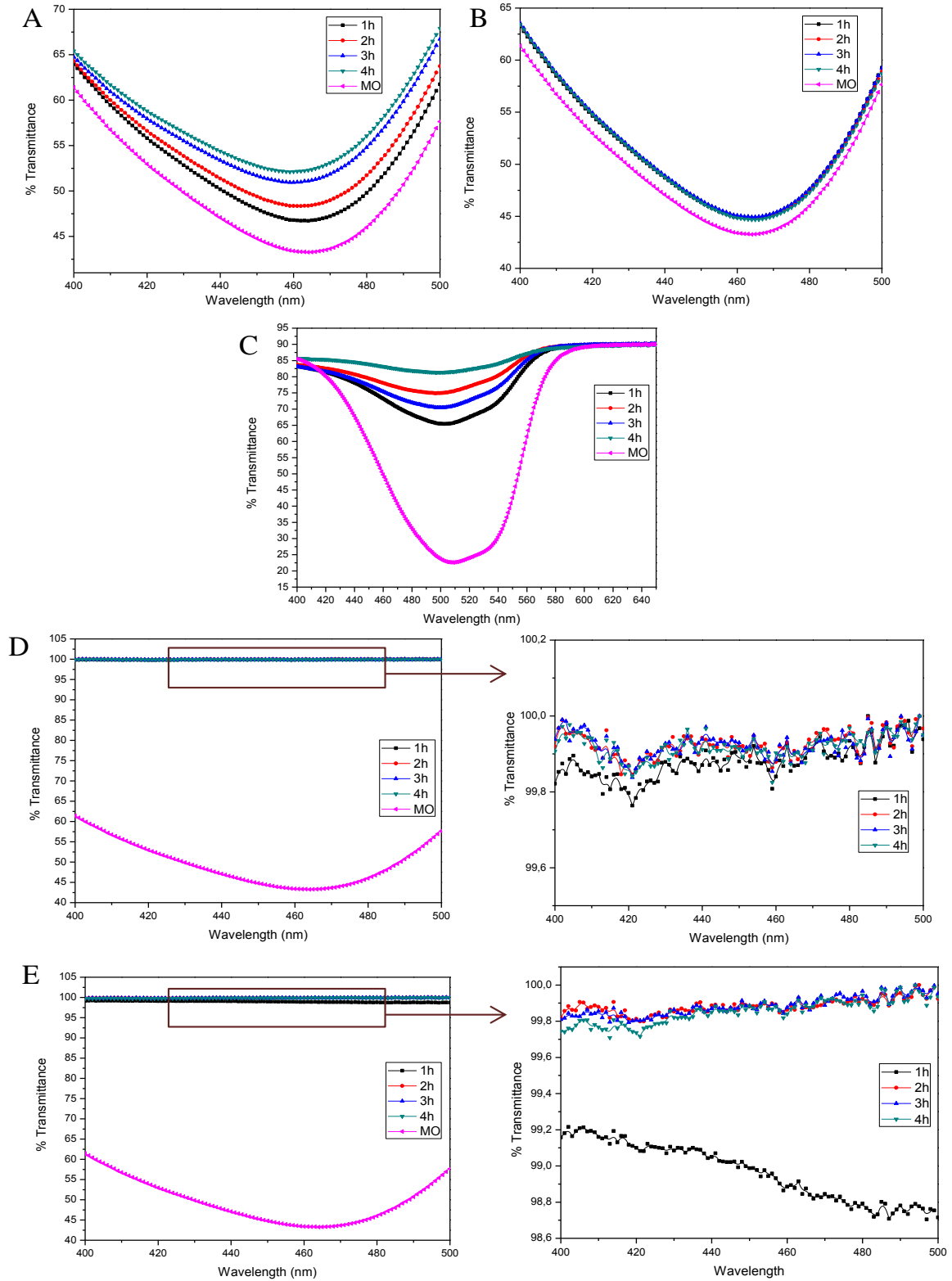
Figure 52. Degradation of MO with different samples. (A) VC_z, (B) VC_f, (C) VC_t, (D) VC_4, (E) VC_5

In relation with the results of degradation of MO under visible light were almost the same as ultraviolet light. The four and five components samples degraded the MO completely in some minutes, faster than in ultraviolet light, for these reason it could not measure the transmittance (%). As the same way, MO was not degraded by ZnO because zincite does not display a high photocatalyitic activity [131] and the presence of zincite crystalline phase in the sample is not very high. The Fe2O3 samples was not degraded too, because of the no presence of crystalline phases. However, the SnO_2 samples were degraded along the time.

In VC_4 with surfactants, the results are similar than VC_{4EtLac} and VC_{4PEG} samples, MO degraded completely in some minutes because of the presence of anatase, although MO is degraded faster in VC_{4PEG} because the the bigger particle size achieved was coupled with better crystallinity [132] [133] than in Etnyllactate samples. However MO was not degraded by VC_4 with Triton X-100 in three hours, T.A.Khalyavka et.al. described that the zinc-containing composites in all cases display greater photocatalytic activity than either pure titanium oxide or zinc oxide [131], it is possible that heating rate or final temperature were not correctly chosen, as result the low crystallinity and big size of zincite crystals.

3. CONCLUSIONS

In summary, TiO_2-SiO_2 sol-gel films with different quantity of ZnO, SnO_2 and Fe_2O_3 were prepared by dip-coating method studying the influence of slow and fast withdrawal rates (60 and 220 mm/min, respectively), number of layers, the influence of surfactants on the coating morphology and their properties by AFM and SEM, crystalline phases by X-ray were analysed.

1. Evaluating the crystalline phases can be establish that:
   a. VC_f with iron presents an amorphous structure, maybe because it needs a higher sintering temperature, as explained in [80].
   b. VC_z and VC_t present zincite and anatase respectively, although the crystal size are 41,68 and 66,07 nm.
   c. VC_5 present anatase and cassiterite as crystalline phases with 60,92 and 117,43 nm as a crystal size.
   d. VC_4 present the same crystal phases than VC_5, but with bigger cassiterite (146,79 nm) and smaller anatase (51,09 nm) particle sizes.

2. The use of surfactants also change the results:
   a. In relation with morphology, they help to avoid the cracks on the surface and improve the homogeneity of the coatings.
   b. The surfactants cause differences in crytallinity, while PEG increase the particle size of anatase (56,57 nm) and casitterite (158,69 nm), Ethylactate causes the opposite (49,50 and 130,48 nm respectively). In addition, Triton X-100 causes the appearance of zincite (148,66 nm) and anatase (36,84 nm) and several zincite aggregates which having size up to 1-5 microns.

3. The morphology of the nanofilms depends of the dip-coating rate and the number of layers in each sol-gel coating:
   a. Three components coatings have differences, although in all of them the thickness and the roughness are bigger at fast rate and 3 layers.
   b. Five components coatings present a bigger roughness than the others because the particles are formed very closely and densely. And the thickness, as the same way, is bigger at fast rate and 3 layers.

c. The roughness in four components is bigger at 1 layer in all samples and it increases considerably with the surfactants were added in the row from lower to higher EtLac>Triton>PEG. And the thickness was the result that it expected, is always thicker at slow rate.

4. Particle size was measured with SEM and AFM, although the AFM results are more accurate using Image Processing v. 2.1 software:

   a. VC_t and VC_z present a smaller particle size at fast rate.

   b. VC_4, as the same way than three components, present the smallest particle size at 220 mm/min.

   c. VC_4 with surfactants (~20-900 nm) present more range in size than VC_4 without surfactants (~60-300 nm). And comparing these data, $VC4_{EtLac}$ has more nanosized and compact particle distribution than the VC_{4PEG} and $VC_{4Triton}$.

5. Regarding to the photocatalytic activity under ultraviolet light:

   a. Three components coatings with ZnO and Fe_2O_3 did not degrade the MO, this phenomenon seems to be due to the absence of crystalline phases (X-ray amorphous). However VC_t degraded MO because of the presence of anatase.

   b. Four and five components coatings present a very good photocatalytic activity; the MO was completely degraded in the first hour in VC_4 case and in the second hour in VC_5.

6. Regarding to the photocatalytic activity under visible light:

   a. The same situation was with three components coatings with ZnO and Fe_2O_3. MO was not degraded by ZnO because zincite does not display a high photocatalyitic activity [131] and the presence of zincite crystalline phase in the sample is not very high. And Fe_2O_3 samples were not degraded too, because of the any presence of crystalline phases. However, the SnO_2 samples were degraded along the time.

   b. Four and five components coatings present a very good photocatalytic activity, the MO was completely degraded immediately in several minutes in both cases.

c. VC_4 with surfactants, also present a good photocatalytic activity under visible light in Ethyllactate and Polyethylene glycol cases because of the presence of anatase, although MO is degraded faster in VC_{4PEG} because the bigger particle size achieved was coupled with better crystallinity than VC_{4EtLac} samples. However MO was not degraded by VC_4 with Triton X-100 in three hours, it is possible that heating rate or final temperature were not correctly chosen, as result the low crystallinity and big size of zincite crystals.

CONCLUSIONES

En resumen, se prepararon láminas con la técnica de dip-coating usando TiO_2-SiO_2 y diferentes cantidades de ZnO, SnO_2 y Fe_2O_3, estudiando la influencia de las velocidades de retirada lenta y rápida (60 y 220 mm/min, respectivamente), número de capas, la influencia de los surfactantes en la morfología y sus propiedades mediante AFM, SEM, y las fases cristalinas que contienen mediante a Rayos X.

1. Evaluando las fases cristalinas se puede establecer:

    a. VC_f con hierro presenta estructura amorfa, porque quizá necesita una temperatura de sintonización más elevada, tal y como se explica en [80].

    b. VC_z y VC_t presentan zincita y anatasa respectivamente, aunque el tamaño del cristal son 41,68 y 66,07 nm.

    c. VC_5 presenta anatasa y casiterita como fases cristalinas con un tamaño de cristal de 60,92 and 117,43 nm.

    d. VC_4 presenta las mismas fases cristalinas que VC_5, pero con un tamaño de cristal mayor en el caso de la casiterita (146,79 nm) y menor en el de la anatasa (51,09 nm).

2. El empleo de surfactantes también produce cambios en los resultados:

    a. Respecto a la morfología, los surfactantes ayudan a evitar las grietas en la superficie y a mejorar la homogeneidad de las láminas.

    b. Los surfactantes también provocan cambios en la cristalinidad, mientras que el PEG incrementa el tamaño de partícula de la anatasa (56,57 nm) y de la caisterita (158,69 nm), el lactato de etilo produce lo contrario (49,50 and 130,48 nm respectivamente). Además, el Triton X-100 produce la aparición de zincita (148,66 nm) y anatasa (36,84 nm) y varios agregados de zincita con un tamaño de partícula entre 1-5 micras.

3. La morfología de las láminas depende de la velocidad de retirada y del número de capas que se le aplique:

    a. Los laminados con tres componentes muestran diferencias entre ellos, aunque en todas ellas el espesor y la rugosidad es mayor a velocidades altas y tres capas.

b. Los revestimientos con cinco componentes presentan mayor rugosidad que el resto porque las partículas aparecen más juntas. Y el espesor, de igual manera, es mayor a velocidad alta y tres capas.

c. La rugosidad in los laminados con cuatro componentes es mayor en los que solo tienen una capa en todas las muestras; esta se incrementa considerablemente cuando se le añaden surfactantes siendo la rugosidad de mayor a menor en EtLac>Triton>PEG. Y, respecto al espesor, se obtuvo el resultado esperado, ya que los laminados son siempre más finos a baja velocidad.

4. El tamaño de partícula fue medido con SEM y AFM, aunque los resultados con AFM fueron más precisos, gracias al uso del software Image Processing v. 2.1:

a. VC_t y VC_z presentan menor tamaño de partícula a baja velocidad.

b. VC_4, de igual forma que los laminados con tres componentes, presenta menor tamaño de partícula a 220 mm/min.

c. VC_4 con surfactantes (~20-900 nm) presenta mayor rango de tamaños que las muestras que no contienen surfactantes (~60-300 nm). Comparando estos resultados $VC4_{EtLac}$ presenta una distribución de partículas más compacta que VC_{4PEG} y $VC_{4Triton}$.

5. En cuanto a la actividad fotocatalítica con luz ultravioleta:

a. Las muestras de tres componentes con ZnO y Fe_2O_3 no degradan el MO, este fenómeno puede ser debido a la ausencia de fases cristalinas (Rayos X es amorfo). Sin embargo, VC_t degrada el MO por la presencia de anatasa.

b. Los laminados con cuatro y cinco componentes presentan a una buena actividad fotocatalítica, el MO fue completamente degradado in la primera hora en el caso de VC_4 y en la segunda en el VC_5.

6. Y en cuanto a la actividad fotocatalítica con luz visible:

a. Ocurre lo mismo que en el caso de luz ultravioleta, las muestras con ZnO y Fe_2O_3 no degradan el MO, porque la zincita no produce una elevada actividad fotocatalítica [131] y la presencia de esta fase cristalina no es muy elevada. Y las muestras con Fe_2O_3 tampoco fueron degradadas, ya que no presentan fase

cristalina. Sin embargo, las muestras de son degradaron el MO a lo largo del tiempo.

b. Las muestras de cuatro y cinco componentes presentan un buena actividad fotocatalítica, puesto que el MO fue completamente degradado inmediatamente en pocos minutos en ambos casos.

c. Las muestras de VC_4 con surfactantes también presentan una buena actividad fotocatalítica bajo la luz visible en los casos que contienen lactato de etilo y PEG, por la presencia de anatasa, aunque el MO fue más rápidamente degradado en VC_{4PEG} debido a su mayor tamaño de partícula con el que se consigue una mejor cristalinidad que en las muestras de VC_{4EtLac}. Sin embargo, el MO no fue degradado por las muestras de VC4 con Triton X-100 a lo largo de 3 horas; es posible que la velocidad de calentamiento o la temperatura final no hayan sido correctamente elegidas, como resultado de la baja cristalinidad y el gran tamaño de los cristales de zincita.

4. BIBLIOGRAPHY

[1] L. Hench Larry and K.West Jon. The Sol-Gel Process. *Chem. Rev*. **1990**, 33-72.

[2] Levy David and Esquivias Luis. Sol-Gel Processing of Optical and Electrooptical Materials. *Adv. Mater*. **1995**, 7, Nº2.

[3] Brinker C.Jeffrey and W.Sherer George. The Physics and Chemistry of Sol-Gel Processing. *ACADEMIC PRESS INC*. **1990**.

[4] Duhua Wang, Gordon. P.Bierwagen. Progress in Organic Coatings. **2009**, 327-338.

[5] B.Figueira Rita, R.Fontinha Isabel, J.R.Silva Carlos and V.Pereira Elsa. Hybrid Sol-Gel Coatings: Smart and Green Materials for Corrosion Mitigation. *Coatings*. **2016**, 6, 12.

[6] K.Malnieks, G.Mezinskis, I.Pavlovska, A. Pludons. Effect of different dip-coating techniques on TiO_2 thin film properties. *Institute of Silicate Materials*. **2009**.

[7] Gundars Mezinskis, Darja Milinkova, Arturs Pludons and Liga Grase. Influence of Substrate Preparation Method on the Morphologies of TiO_2 Sol-Gel Derived Coatings. *Instute of Silicate Materials*. **2015**.

[8] R. Parra, M. S. Góes, M. S. Castro, E. Longo, P. R. Bueno, and J. A. Varela. Reaction Pathway to the Synthesis of Anatase via the Chemical Modification of Titatinum Isopropoxide with Acetic Acid. *Chem. Mater*. **2008**, 20, 143-150.

[9] N. Mastali, H. Bakhtiari. Investigation on the structural, morphological and photochemical properties of spin-coated TiO_2 and ZnO thin films prepared by sol-gel method. *International Journal of Nano Dimension.* **2014**, 113-121.

[10] Nur Syahraain Zulkiflee, Rosniza Hussin, Jumrah Halim, Mohd Izham Ibrahim, Mohamad Zulhafizi Zainal, Shahzua Nizam and Suhailah Abdul Rahman. Characterization of TiO_2, ZnO, and TiO_2/ZnO thin films prepared by sol.gel method. *Journal of Engineering and Applied Sciences*. **2016**, Nº12

[11] Daniela Cordeiro Leite Vasconcelos, Vilma Conceiçâo, Eduardo Henrique Martins Nunes, Antônio Claret Soares Sabioni, Massimo Gasparon, Wander Luiz Vasconcelos.

Infrared Spectroscopy of Titania Sol-Gel Coatings on 316L Stainless Steel. *Materials Sciences and Application.* **2011**, 2, 1375-1382.

[12] Ayodele Abeeb Daniyan, Lasisi Ejibunu Umoru, Bankole Olunlade. Preparation of Nano-TiO$_2$ Thin Films Using Spin Coating Method. *Journal of Minerals and Materials Characterization and Engineering*. **2013**, 1, 138-144.

[13] V.Anand Ganesh, A.Sreekimaran Nair, Hemant Kumar Raut, Timothy Michael Walsh and Seeram Ramakrishna. Photocatalytic superhydrophilic TiO2 coating on glass by electrospinning. *RSC Adv*. **2012**, 2, 2067-2072.

[14] Anna Eremenkp, Natalia Smirnova, Iurii Gnatiuk, Oksana Kinnik, Nadezhda Vityuk, Iuliia Mukha and Aleksander Korduban. Silver and Gold Nanopartilces on Sol-Gel TiO$_2$, ZrO$_2$, SiO$_2$ Surfaces: Optical Spectra, Photocatalytic Activity, Bactericide Properties.

[15] Pablo Galliano, Juan José Damborenea, M Jesús and Alicia Durán. Sol-Gel Coatings on 316L Steel for Clinical Application. *Journal of Sol-Gel Science and Technology*. **1998**, 13,723-727.

[16] S. Abedrabbo, B. Lahlouh, S. Shet, A. T. Fiory and N. M. Ravindra. Spin-Coated Erbium-Doped Silica Sol-Gel Films on Silicon.

[17] Emöke Volentiru, Mária Nyári, Gabriella Zoltán Hórvölgyi, Liana MariaMuresan. Silica sol-gel protective coatings against corrosion of zinc substrates. *Periodica Polytechnica*. **2014**, 61-66.

[18] V. Skroznikova, N. Popovich, Ts. Dimitrov. Transparent hydrophobic sol-gel silica coatings on glass. **2013**, 52.

[19] C. A. Milea, C. Bogatu, A.Duta. The influence of parameters in silica sol-gel process. *Engineering Sciences.* **2011**, Nº1.

[20] B. Gündüz, M. Cavas, F. Yakuphanoglu. Quality Controlling of SiO$_2$ Thin Films by Sol Gel Method. *International Advanced Technologies Symposium.* **2011**.

[21] Xiaoguang Li, Liping Zou, Guangming Wu, Jun Shen. Laser-induced damage on ordered and amorphous sol-gel silica coating.

[22] B. Kaleji, M. Mousaei, H. Halakouie, A.Ahmadi. Sol-gel Synthesis of ZnO Nanoparticles and ZnO-TiO$_2$-SiO$_2$ Nanocomposites and Their Photo-catalyst Investigation in Methylene Blue Degradation. **2015**, 219-225.

[23] B.W. Shivaraj, H.N. Narasimha Murthy, M. Krishna, B.S. Satyanarayana. Effect of Annealing Temperature on Structural and Optical properties of Dip and Spin coated ZnO Thin Films. *Procedia Materials Science.* **2015**, 292-300.

[24] E. Bacaksiz, M. Parlak, M. Tomakin, A. Özçelik, M. Karakiz, M. Altunbas. The effects of zinc nitrate, zinc acetate and zinc chloride precursors on investigation of structural and optical properties of ZnO thin films. *Journal of Alloys and Compounds 466.* **2008**, 447-450.

[25] P. Periyat, S.G. Ullattil. Sol-gel derived nanocrystalline ZnO photoanode film for dye sensitized solar cells. *Material Science in Semiconductor Processing.* **2015**, 139-146.

[26] X.L. Cheng, H.Zhao, L.H. Huo, S. Gao, J.G. Zhao. ZnO nanoparticulate thin film: preparation, characterization and gas-sensing property. *Sensors and Actuators B.* **2004**, 102, 248-252.

[27] Min Guo, Peng Diao, Shengmin Cai. Hydrothermal growth of well-aligned ZnO nanorod arrays: Dependence of morphology and alignment ordering upon preparing conditions. *Journal of Solid State Chemistry.* **2005**, 178, 1864-1873.

[28] Jianguo LV, Wanbing Gong, Kai Huang, Jianbo Zhu, Fanming Meng, Xueping Song, Zhaoqi Sun. Effect of annealing temperature on photocaralytic activity of ZnO thin films prepared by sol-gel method. *Superlattices and Microstructures.* **2011**, 50, 98-106.

[29] Clemente Luyo, Ismael Fábregas, L. Reyes, José L. Solís, Juan Rodríguez, Walter Estrada, Roberto J. Candal. SnO2 thin-films prepared by spray-gel pyrolisis: Influence of sol properties on film morphologies. *Thin Solid Films*. **2007**, 516, 25-33.

[30] Sang Ho Lee, David M. Hoffman, Allan J. Jacobson and T. Randall Lee. Transparent, Homogeneous Tin Oxide (SnO2) Thin Films Containing SnO2-Coated Gold Nanoparticles. *Chemistry of Materials*. **2013**, 25, 4697-4702.

[31] Zhao Jie, Huo Li-Hua, Gao Shan, Zhao Hui, Zhao Jing-Gui. Alcohols and acetone sensing properties of SnO_2 thin films deposited by dip-coating. *Sensors and Actuators.* **2006**, 115, 460-464.

[32] Muhammad Akhyar FARRUKH, Boon-Teck HENG, Rohana ADNAN. Surfactant-controlled aqueous synthesis of SnO_2 nanoparticles via the hydrothermal and conventional heating methods. *Turk J Chem.* **2010**, 34, 537-550.

[33] Tao JIN, Fan-mei KONG, Rui-qin BAI, and Ru-liang ZHANG. Anti-corrosion mechanism of epoxy-resin and different content Fe2O3 coatings on magnesium alloy. *Front. Mater. Sci.* **2016**.

[34] Abdolreza Nilchi, Simin Janitabar-Darzi, Somayeh Rasouli-Garmarodi. Sol-Gel Preparation of Nanoscale TiO_2/SiO_2 Composite for Eliminating of Con Red Azo Dye. *Materials Science and Applications.* **2011**, 2, 476-480.

[35] Magali Bonne, Stéphane Pronier, Yann Batonneau, Fabien Can, Xavier Courtois, Sébastien Royer, Patrice Marécot and Daniel Duprez. Surface properties and thermal stability of SiO_2- crystalline TiO2 nano-composites. *Journal of Materials Chemistry.* **2010**, 20, 9205-9214.

[36] Liyun Chen, Xiaoping Liao, Weizhong Jiang, Jiayi Ye, Huile Jin, Aili Liu. Preparation and Properties of TiO_2/SiO_2 Thin Films on Enamel Substrates. *Material Science Forum.* **2016**, 848, 717-721.

[37] Najme lari, Shahrokh Ahangarani and Ali Shanaghi. Effect of Different TiO_2-SiO_2 Multilayer Coatings Applied by Sol-Gel Method on Antireflective Property. *Journal of Materials Engineering and Performance.* **2015**, 24, 7.

[38] A. Shokuhfar, M. Alzamani, E. Eghdam, M. Karimi, S. Mastali. SiO_2-TiO_2 Nanostructure Films on Windshields Prepared by Sol-Gel Dip-Coating Technique for Self-Cleaning and Photocatalytic Applications. *Nanoscience and Nanotechnology.* **2012**, 2, 16-21.

[39] Shaozheng Hu, Fayun Li and Zhiping Fan. Preparation of SiO_2-Coated TiO_2 Composite Materials with Enhanced Photocatalytic Activity Under UV Light. *Bull. Korean Chem. Soc.* **2012**, 33, N°6.

[40] Sanjay S. Latthe, Shanhu Liu, Chiaki Terashima, Kazuya Nakata Akira Fujishima. Transparent, Adherent, and Photocatalytic SiO_2-TiO_2 Coatings on Polycarbonate for Self-Cleaning Applications. *Coatings.* **2014**, 4, 497-507.

[41] Yuri Hendrix, Alberto Lazaro, Qingliang Yu, Jos Brouwers. Titania-Silica Composites: A Review on the Photocatalytic Activity and Synthesis Methods. *World Journal of Nano Science and Engineering.* **2015**, 5, 161-177.

[42] Meshal S.Al-Johani, Yousef S.Al-Zaghayer, Sulaiman I.Al-Mayman. TiO_2-ZnO Photocatalytic Activity for Hydrogen Production. *International Scienctific Journal Environmental Science.*

[43] Chun Cheng, Abbas Amini, Chao Zhu, Zuli Xu, Haisheng Song, Ning Wang. Enhanced photocatalytic performance of TiO_2-ZnO hybrid nanostructures. *Scientific Reports.* **2014.**

[44] Razan Fateh, Ralf Dillert and Detlef W Bahnmann. Self-Cleaning Properties, Mechanical Stability, and Adhesion Strength of Transparent Photocatalytic TiO2-ZnO Coatings on Polycarbonate. *Applied Materials and Interfaces.* **2014**.

[45] Gregorio F. Ortiz, Ilie Hanzu, Pedro Lavela, Philippe Knauth, José L. Tirado and Thierry Djenizian. Nanoarchitectured TiO_2/SnO: A Future Negative Electrode for High Power Density Li-Ion Microbatteries. *Chemistry of Materials.* **2010**, 22, 1926-1932.

[46] Zhaoyue Liu, Kai Pan, Meijia Wang, Min liu, Qiang Lü, Yubai Bai, Teijin Li. Influence of the mixed ratio on the photocurrent of the TiO2/SnO2 composite photoelectrodes sensitized by mercurochrome. *Journal of Photochemistry and Photobiology.* **2003**, 157, 39-46.

[47] Zhaoyang Liu, Darren Delai Sun, Peng Guo and James O. Leckie. An Efficient Bicomponent TiO2/SnO2 Nanofiber Photocatalyst Fabricated by Electrospinning with a Side-by-Side Dual Spinneret Method. *American Chemical Society.* **2006**, Nº4, 1081-1085.

[48] Savas Sönmezoglu, Aysun Arslan, Tülay Serin and Necmi Serin. The effects of film thickness on the optical properties of TiO_2-SnO_2 compound thin films. *Physica Scripta.* **2011**.

[49] Changhua Wang, Changlu Shao, Xintong Zhang and Yichun Liu. SnO$_2$ Nanostructures-TiO$_2$ Nanofibers Heterostructures: Controlled Fabrication and High Photocatalyitic Properties. *Inorganic Chemistry.* **2009**, 48, 7261-7268.

[50] M.-J. Zhou, Z.-O. Zeng and L. Zhong. Energy storage ability and anti-corrosion proptection properties of TiO$_2$-SnO$_2$ system. *Materials and Corrosion.* **2010**, 61, N°4.

[51] Wenwei Tang, Lujun Wu, Xiaoying Chen and Xinping Zeng. Degradation of Rhodamine B with Visivle Light Response of Fe$_2$O$_3$/TiO$_2$ Film Electrode. *ECS Journal of Solid State Science and Technology.* **2014**, 3, Q69-Q73.

[52] E. Celik, A. Y. Yildiz, N.F. Ak Azem, M. Tanoglu, M. Toparli. Preparation and characterization of Fe$_2$O$_3$-TiO$_2$ thin films on glass substrate for photocatalytic application. *Materials Science and Engineering.* **2006**, 129, 193-199.

[53] Kathryn E. Dekrafft, Cheng Wang and Wenbin Lin. Metal-Organic Framework Templated Synthesis of Fe$_2$O$_3$/TiO$_2$ Nanocomposite for Hydrogen Production. *Advanced Materials.* **2012**, 24, 2014-2018.

[54] Peng Luan, Mingzheng Xie, Xuedong Fu, Yang Qu, Xiaojun Sun and Liqiang Jing. Improved photoactivities of TiO$_2$/Fe$_2$O$_3$ nanocomposites for visible-light water splitting after phosphate bridging and mechanism. *Physical Chemistry and Chemical Physics.*

[55] Xingwang Zhang, Lecheng Lei. Preparation of photocatalytic Fe$_2$O$_3$-TiO$_2$ coatings in one step by metal organic chemical vapour deposition. *Applied Surface Science.* **2008**, 254, 2406-2412.

[56] Jing Zhai, Xia Tao, Yuan Pu, Xiao-Fei Zeng, Jian-Feng Chen. Core/shell structured ZnO/SiO$_2$ nanoparticles: Preparation, characterization and photocatalytic property. *Applied Surface Science.* **2010**, 257, 393-397.

[57] Jun Bo Zhong, Jian Zhang Li, Xi Yang He, Jun Zeng, Yan Lu, Jin Jin He and Fei Zhong. Fabrication and Catalytic Performance of SiO$_2$-ZnO Composite Photocatalysy. **2013**.

[58] Lívia Naszályi, Florence Bosc, Abdeslam El Mansouri, Arie van der Lee, Didier Cot, Zoltán Hórvölgyi, André Ayral. Sol-gel-derived mesoporous SiO$_2$/ZnO active

coating and development of multifunctional ceramic membranes. *Separation and Purification Technology.* **2008**, 59, 304-309.

[59] Nazanin Farhadyar, Mirabdullah Seyed Sadjadi. Synthesis and Characterization of ZnO-SiO$_2$/Epoxy Nanocomposite Coating by Sol-gel Process. *Journal of Nano Research.* **2011**, 16, 1-7

[60] K T Simfroso, A C Alguno, F R Bagsican, M E Jabian, M K G Odarve, G G Paylaga, B R B Sambo, R M Vequizo and R T Candidato. Growth mechanism of chemically prepared ZnO-SiO$_2$ nanostructures grown on glass and silicon substrates. *Materials Science and Engineering.* **2015**, 79.

[61] Lan Shangping, Jia Hongzhi, Jiang Daoping, Lu Huancai. Large photosensitivity in SnO$_2$/SiO$_2$ thin film fabricated by sol-gel method. *Optoelectronis and advanced materials.* **2012**, 6, N° 1-2, 288-291.

[62] G. Granger, C. Restoin, P. Roy, R. Jamier, S. Rougier, A. Lecomte, J.-M. Blondy. Nanostructured optical fibers in the SiO$_2$/SnO$_2$ system by the sol-gel method. *Materials Letters.* **2014**, 120, 292-294.

[63] J. Del Castillo, A. C. Yanes, J. Méndez and V. D. Rodríguez. Luminescence of Nanostructured SnO$_2$-SiO$_2$ Glass- Ceramics Prepared by Sol-Gel Method. *Journal of Nanoscience and Nanotechnology.* **2008**, 8, 2143-2146.

[64] Yunshi Liu, Ping Yang, Jia Li, Katarzyna Matras-Postolek, Yunlong Yue Baibiao Huang. Formation of SiO$_2$@SnO$_2$ Core-Shell Nanofibers and Their Gas Sensing Properties. *The Royal Society of Chemistry.* **2013**, 1-3

[65] Zhijie Li, Wenzhong Shen, Zhiguo Wang, Xia Xiang, Xiaotao Zu, Qiangmin Wei, Lumin Wang. Direct formation of SiO$_2$/SnO$_2$ composite nanoparticles with high surface area and high thermal stability by sol-gel hydrothermal process. *Journal Sol-Gel Science Technology.* **2009**, 49, 196-201.

[66] Aili Wang, Chaoqun Ge, Henbo Yin, Min Ren, Yunsheng Zhang, Quanfa Zhou, Zhanao Wu, Jichuan Huo, Xian Li, Tingshun Jiang. Evolution of binary Fe$_2$O$_3$/SiO$_2$ coating layers on the surfaces of aluminium flakes and the pigmentary performances. *Powder Technology.* **2012**, 221, 306-311.

[67] A. Teleki, M. Suter, P.R. Kidambi, O. Ergeneman, F. Krumeich, B.J. Nelson and S.E. Pratsinis. Hermetically-Coated Superparamagnetic Fe_2O_3 Particles with SiO_2 Nanofilms. *Nanotech.* **2009**, 1.

[68] Ri Yu, Juyeon Yun, Jae-Hwan Pee, Yoojin Kim. Design of a bi-functional α-Fe_2O_3/Zn_2SiO_4:Mn_2+ by layer-by-layer assembly method. *Archives of Metallurgy and Materials.* **2014**.

[69] M. Raileanu, M.Crisan, C. Petrache, D.Crisan, M. Zaharescu. Fe_2O_3-SiO_2 nanocomposites obtained by different sol-gel routes. *Journal of Optoelectronics and Advanced Materials.* **2003**, 5, N°3, 693-698.

[70] M. K. Verma, V. Gupta. Highly sensitive ZnO-SnO_2 nanocomposite H_2 gas sensor. *The 14th International Meeting on Chemical Sensors.* **2012**.

[71] R.A. Zargar, M.A. Bhat, I.R. Parrey, M. Arora, J. Kumar and A.K. Hafiz. Optical properties of ZnO/SnO_2 composite coated film. *Optics.* **2016.**

[72] Abdessalem Hamrouni, Noomen Moussa, Francesco Parrino, Agatino Di Paola, Ammar Houas, Leonardo Palmisaon. Sol-gel synthesis and photocatalytic activity of ZnO-SnO_2 nanocomposites. *Journal of Molecular Catalysis A: Chemical.* **2014**, 390, 133-141.

[73] S. Mihaiu, I. Atkinson, M. Anastasescu, A. Toader, M. Voicescu and M. Zaharescu. Nanostructured Zn-Sn-O films obtained by dip-coating technique.

[74] Gaël Giusti, Vincent Consonni, Etienne Puyoo and Daniel Bellet. High Performance ZnO-SnO_2:F Nanocomposite Transparent Electrodes for Energy Applications. *Applied Materials and Interfaces.*

[75] Suresh Kumar, Ravi Nigam and Virender Kundu. Sol-gel synthesis of ZnO-SnO_2 nanocomposites and their morphological, structural and optical properties. *Journal Material Science.* **2015**.

[76] Yanjun Liu, Li Sun, Jiagen Wu, Ting Fang, Ran Cai, Ang Wei. Preparation and photocatalytic activity of ZnO/Fe_2O_3 nanotube. *Material Science and Engineering B.* **2015**, 194, 9-13.

[77] M.A. Valenzuela, P.Bosch, J. Jiménez-Becerril, O. Quiroz, A.I. Paéz. Preparation, characterization and photocatalytic activity of ZnO, Fe_2O_3 and $ZnFe_2O_4$. *Journal of Photochemistry and Photobiology A: Chemistry.* **2002**, 148, 177-182.

[78] Lek Sikong, Kalayanee Kooptarnond, Sutham Nyonwas and Jiraporn Damchan. Photoactivity and hydrophilic property of SiO_2 and SnO_2 co-doped TiO_2 nano-composite thin films. *Songklanakarin Journal of Science and Technology.* **2010**, 32 (4), 413-418.

[79] Chao Song, Xiangting Dong. Preparation and Characterization of tricomponent $SiO_2/SnO_2/TiO_2$ composite nanofibers by electrospinning. *Optoelectronics and Advanced Materials.* **2012**, 6, Nº1-2, 225-229.

[80] Hongtao Cui, Wanzhong Ren and Wenhua Wang. Highly transparent UV absorption TiO_2-SiO_2-Fe_2O_3 films without oxidation catalytic activity prepared by a room temperature sol-gel route. *Journal Sol-Gel Science Technology.* **2011**, 58, 476-480.

[81] Jesús I Peña-Flores, Abraham F Palomec-Garfias, César Márquez-Beltrán, Enrique Sánchez-Mora, Estela Gómez-Barojas and Felipe Pérez-Rodríguez. Fe effect on the optical properties of TiO_2:Fe_2O_3 nanostructured composites supported on SiO2 microsphere assemblies. *Nanoscale Research Letters.* **2014**.

[82] Chao Song, Xiangting Dong. Preparation and Characterization of Tetracomponent $ZnO/SiO_2/SnO_2/TiO_2$ Composite Nanofibers by Electrospinning. *Advances in Chemical Engineering and Science.* **2012**, 2, 108-112.

[83] R.Vidhya, M. Sankareswari, K. Neyvasagam. Effect of annealing temperature on structural and optical properties of Cu-TiO_2 thin film. *International Journal of Technical Research and Applications.* **2016**, 37, 42-46.

[84] S. Doeuff, M. Henry, C. Sanchez. Hydrolysis of titanium alkoxides: Modification of the molecular precursor by acetic acid. *Journal of Non-Crystalline Solids.* **1987**, 89, 206-216.

[85] Xueli Cheng, Dairong Chen and Yongjun Liu. Mechanism of Silicon Alkoxide Hydrolysis-Oligomerization Reactions: A DFT Investigation. *ChemPhysChem.* **2012**, 0, 1-14.

[86] Agnieszka Smieszek, Anna Donesz-Sikorska, Jakub Grzesiak, Justyna Krzak and Krzysztof Marycz. Biological effects of sol-gel derived ZrO_2 and SiO_2/ZrO_2 coatings on stainless steel surface- In vitro model using mesenchymal stem cells. *Journal of Biomaterials Applications.* **2014**,

[87] N. V. Kaneva, C. D. Dushkin. Preparation of nanocrystalline thin films of ZnO by sol-gel dip-coating. *Bulgarian Chemical Communications.* **2011**, 2, 259-263.

[88] Zohra Nazir Kayani, Maryam Iqbal, Saira Riaz, Rehana Zia, Shahzad Naseem. Fabrication and properties of zinc oxide thin film prepared by sol-gel dip coating method. *Material Science-Poland.* **2015**, 33 (3), 515-520.

[89] Sekhar C. Ray, Malay K. Karanjai, Dhruba DasGupta. Tin dioxide based transparent semiconducting films deposited by the dip-coating technique. *Surface and Coatings Technology.* **1998**, 102, 73-80.

[90] Daoli Zhang, Liang Tao, Zhibing Deng, Jianbing Zhang, Liangyan Chen. Surface morphologies and properties of pure and antimony-doped tin oxide films derived by sol-gel dip-coating processing. *Materials Chemistry and Physics.* **2006**, 100, 275-280.

[91] Zohra Nazir Kayani, Erum Shahid Khan, Farhat Saleemi, Saira Riaz and Shahzad Naseem. Growth and Characterization of Iron Oxide Nanocrystalline Thin Films via Sol-Gel Dip Coating Method. *IEEE Transactions on Magnetics.* **2014**, 8.

[92] Toxicology and Carcinogenesis Studies of Diethanolamine (CAS No. 111-42-2) in F344/N Rats and B6C3F1 Mice (Dermal Studies). *National Toxicology Program.* **1999**.

[93] Masashi Ohyama, Hiromitsu Kozuka, Toshinobu Yoko. Sol-gel preparation of ZnO films with extremely preferred orientation along (002) plane from zinc acetate solution. *Thin Solid Films.* **1997**, 306, 78-85.

[94] Min Guo, Peng Diao, Shengmin Cai. Hydrothermal growth of well-aligned ZnO nanorod arrays: Dependence of morphology and alignment ordering upon preparing conditions. *Journal of Solid State Chemistry.* **2005**, 178, 1864-1873.

[95] M. Vishwas, K. Narasimha Rao, K.V. Arjuna Gowda, R.P.S Chakradhar. Influence of Sn doping on structural, optical and electrical properties of ZnO thin films prepared by cost effective sol-gel process. *Spectrochimica Acta Part A.* **2012**, 95, 423-426.

[96] R. Vidhya, M. Sankareswari, K. Neyvasagam. Efect of Annealing Temperature on Structural and Optical Properties of Cu-TiO₂ Thin Film. *International Journal of Technical Research and Applications.* **2016**, 37, 42-46.

[97] Burlakova Aleksandra. Sola-Gela Al2O3-SiO2-TiO2 Biezie Parklajumi. *Magistra darbs.* **2013**.

[99] CHAI Li-yuan, YU Yan-fen, ZHANG Gang, PENG Bing, WEI Shun-wen. Effect of surfactants on preparation of nanometer TiO2 by pyrohydrolisis. *Transantions of Nonferrous Metals Society of China.* **2007**. 17, 176-780.

[100] Inseok Jang, Hui Jun Leong and Seong-Geun Oh. Effects of surfactants on the preparation of TiO2 nanoparticles in microwave-assisted sol-gel porcesss and their photocatalytic activity. *Korean J. Chem. Eng.* **2016**.

[101] Urh Cernigoj, Urska Lavrencic Stangar, Poloonca Trebse, Ursa Opara Krasovec, Silvia Gross. Photocatalytically active TiO2 thin films produces by surfactant-assisted sol-gel processing. *Thin solid Films.* **2006**. 495, 327-332.

[102] Ommeaymen Sheikhnejad-Bishe, Feng Zhao, Ali Rajabtabar-Darvish, Erfan Khodadad, Ali Mostofizadeh and Yudonf Huang. Influence of temperature and surfactants on the photocatalytic performance of TiO2 Nanoparticles. *Int. J- Electrochem. Sci.* **2014**. 9, 4230-4240.

[103] Sanjan Choudhary, Man Singh, R. K. Kale. Surfactant-catalyzed SiO2 thin films preparation and characterization. *Journal of Adhesion Science and Technology.* **2013**.

[104] C.C. Vidyasagar, Y. Arthoba Naik. Surfactant (PEG 400) effects on crystallinity of ZnO nanoparticles. *Arabian Journal of Chemistry.* **2012**.

[105] T. Thilagavathi, D. Geetha. Nano ZnO structures synthesized in presence of anionic and cationic surfactant under hydrothermal process. *Appl Nanosci.* **2012**.

[106] Jamil Kamal Salem, Talaat Moussa Hammad. The effect of surfactants on the particle size and optical properties of precipitated ZnO nanoparticles. *Journal of Materials Science and Engineering.* **2009**. 3, Nº12.

[107] Mi Wang, Yanfeng Gao, Lei Dai, Chuanxiang Cao, Xuhong Guo. Influence of surfactants on the morphology of SnO2 nanocrystals prepared via hydrothermal method. *Journal of Solid State Chemistry*. **2012**. 189, 49-56.

[108] J. Gajendiran and V. Rajendran. Different surfactants assisted on the synthesis of SnO2 nanoparticles and their characterization. *International Journal of Materials and Biomaterials Applications.* **2012**. 2, 37-40.

[109] Amir Memar, Chi M- Phan, Moses O. Tade. Influence of surfactants on Fe2O3 nanostructure photoanode. *International Journal of Hydrogen Energy.* **2012**. 37, 6835-6843.

[110] Guozhong Gao. Nanostructures & Nanomaterials. Synthesis, Properties & Applications. *Imperial College Press.* **2004**.

[111] Krishna Seshan. Handbook of Thin-Film Deposition Processes and Techniques. Principles, Methods, Equipment and Applications. *Noyes Publications*. **2002**.

[112] M. N. Rahaman. Ceranic Processing and Sintering. *Marcel Dekker, Inc.*

[113] Gundars Mezinskis, Darja Milinkova, Arturs Pludons and Liga Grase. Influence of Substrate Preparation Method on the Morphologies of TiO2 Sol-Gel Derived Coatings. *Advanced Materials Research.* Vol. 1117, 143-146.

[114] Kaspars Malnieks, Gundars Mezinskis. Optical, Photocatalytical and Structural Properties of TiO2-SiO2 Sol-Gel Coatings on High Content SiO2 Enamel Surface. *ISSN 1392 MATERIALS SCIENCE (MEDŽIAGOTYRA)*. **2015**. Vol. 21, Nº 1.

[115] M.S. Abd-Elhady, S.I.M Zayed and C.C.M Rindr. Removal of dust particles form the surface of solar cells and solar collectors using surfactants. *International conference on Heat Exchanger Fouling and Cleaning.* **2011**. 343-348.

[116] I.Pavlovska. Drying and Sintering technique. *Riga Technique University.*

[117] WiTec. Atomic Force Microscopes- Nanoscale Surface Characterization.

[118] Robert A. Wilson and Heather A. Bullen. Basic Theory- Atomic Force Microscopy (AFM). *Introduction to Scanning Probe Microscopy (SPM).*

[119] Dattuprasad Ramanlal Joshi. Engineering Physics. *M S University of Baroda.* **2010**.

[120] Jim Schweitzer. Scanning Electron Microscope- Radiological and Environmental Management. *Purdue University*.

[121] Juan Carlos Correa Zapata, Cristian David Aguire Hernández. Obtención, caracterización y actividad fotocatalítica del óxido de titanio dopado con nitrógeno a partir de urea y nitrato de amonio para su tuilización en la region del visible del espectro electromagnetic. *Universidad Tecnológica de Pereira.* **2014**.

[122] Tianzhong Tong, Jinlong Zhang, Baozhu Tian, Feng Chen, Dannong He. Preparation of Fe3+-doped TiO2 catalyst by controlled hydrolysis of titanium alkoxide and study on their photocatalytic activity for methyl orange degradation. *Journal of Hazardous Materials.* **2008**. 155, 572-579.

[123]D.L. Liao, C.A. Badour, B.Q. Liao. Preparation of nanosized TiO2/ZnO composite catalyst and its photocatalytic activity for degradation of methyl orange. *Journal of Photochemistry and Photobiology.* **2008**. 194, 11-19.

[124] Jing Cao, Bange Luo, Haili Lin, Benyan Xu, Shifu Chen. Visible light photocatalytic activity enhancement and mechanism of AgBr/Ag3PO4 hybrids for degradations of methyl orange. *Journal of Hazardous Materials.* **2012**. 217-218, 107-115.

[125] Barbara L Dutrow, Christine M. Clark. X-ray Powder Diffraction (XRD) *Geochemical Instrumentation and Analysis.*

[126] W. W. Norton, Muskingum University web page. Available in: http://www.muskingum.edu/~ericlaw/pd_courses/geol101/minerals/minImages/minImages-Pages/Image11.html

[127] Robert Riehn, Neil Kad, Patricia Opresko, Ingrid Tessmer. Physics college of North Carolina State University. Available in: https://www.physics.ncsu.edu/wang/

[128] Meghan Manning. Atomic Force Microscopy Lecture 7 Outline 1. Available in: http://slideplayer.com/slide/9702681/

[129] Jonathan Atteberry. The key Components of a Scanning Electron Microscope. Available in: http://science.howstuffworks.com/scanning-electron-microscope2.htm

[130] Miramar College. UV Visible Absorption Spectroscopy. Available in: http://faculty.sdmiramar.edu/fgarces/LabMatters/Instruments/UV_Vis/Cary50.htm

[131] T. A. Khalyavka, E. I. Kapinus, T. I. Viktorova and N. N. Tsyba. Adsorption and Photocatalytic Properties of Nanodimensional Titanium-Zinc oxide composites. *Theoretical and Experimental Chemistry.* **2009**. Vol. 45, Nº4.

[132] Paola Calza, Ezio Pelizzetti, Károly Mogyorósi, Robert Kin, Imre Dékány. Size dependent photocatalytic activity of hydrothermally crystallized titania nanoparticles on poorly adsorbing phenol in absence and presence of fluoride. *Applied catalysis B: Environmental.* **2006**. Volume 72, 314-321.

[133] Xinyu Zhang, Jiaqian Qin, Yanan Xue, Pengfei Yu, Bing Zhang, Limin Wang and Riping Liu. Effect of aspect ratio and surface defects on the photocatalytic activity of ZnO nanorods. *Scientific reports.* **2014**.

5. APPENDICES

In this appendice is shown the method to measure the average roughness, bearing ratio, surface area and thickness.